PAPER

Exact conservative solutions of fluid models for the scrape-off layer as the ancestors of plasma blobs?

IOP ebooks™

Bringing you innovative digital publishing with leading voices to create your essential collection of books in STEM research.

Start exploring the collection - download the first chapter of every title for free.

Exact conservative solutions of fluid models for the scrape-off layer as the ancestors of plasma blobs?

João P.S. Bizarro[ORCID], Luís Venâncio and R. Vilela Mendes[a]

Instituto de Plasmas e Fusão Nuclear, Instituto Superior Técnico, Universidade de Lisboa,
1049-001 Lisboa, Portugal

E-mail: bizarro@ipfn.tecnico.ulisboa.pt

Abstract

New exact, analytical solutions are presented for the conservative part of a standard two-fluid (density plus vorticity) model of the scrape-off layer (SOL) which are of the travelling-wave type and describe the transport of large, machine-scale structures across a plasma cross-section (radially and/or poloidally). It is conjectured that amongst these conservative solutions (some extended throughout space, others much more localised) might be the ancestors of propagating coherent structures, known as blobs, often seen in experiments and numerical simulations of SOL turbulence. Several types of solutions can be obtained, capable of mimicking not only high-density blobs propagating outwards, but also inwardly moving plasma holes (structures with densities lower than the backrgound's). Besides their fundamental interest as conservative solutions of the equations describing SOL turbulence, these exact solutions have the added value of providing benchmarks for the verification of numerical algorithms, as is here illustrated. Having thus verified one's numerical implementation, a more realistic SOL model (including diffusion, parallel losses and a source of core plasma) is solved (by gradually adding the extra terms to the conservative part) to check whether these conservative solutions survive the full dynamics or not. They actually do survive (albeit enduring some degree of distortion, ending up by being eventually lost) for parameters representative of SOL plasmas in present-day fusion devices, thus somewhat vindicating one's original conjecture that they might be the ancestors of blobs. In addition, being actual solutions of the conservative part of the fluid SOL equations (and with the possibility of taking essentially Gaussian forms), there is no need to further justify their use as seeds with which to initialise (so-called seeded) simulations. A further characteristic that these Gaussian, blob-like conservative solutions possess is that they have intrinsic net vorticity (or spin), which is also believed to be the case for turbulence-created blobs.

Keywords: plasma blobs, scrape-off layer, tokamaks, two-field model

(Some figures may appear in colour only in the online journal)

1. Introduction and motivation

The behavior and properties of so-called blobs, which are large-scale, coherent structures that are intermittently transported across the scrape-off layer (SOL) of fusion devices, are well documented both experimentally and numerically [1–19]. A good theoretical comprehension already exists regarding the mechanisms by which blobs are transported across the SOL [1–6, 8, 9, 12–21], and their life cycle (from their generation to their convective, ballistic transport and ejection from the plasma) has been reproduced in numerical simulations [3–5, 9, 12, 15]. However, analytical insight on how blobs actually

---

[a] Also at: Centro de Matemática, Aplicações Fundamentais e Investigação Operacional, Universidade de Lisboa, Portugal.

originate and form remains scarce [9, 13, 22], with many simulations still being conducted with recourse to seeded blobs (usually with a Gaussian shape) in a background plasma [2, 6, 9, 13–19], which justifies the current interest devoted to the physics behind the formation and origin of plasma blobs [22, 23]. The purpose of this paper is to focus on a recent conjecture on the origin of blobs, according to which the ancestors of blobs might be the solutions of the conservative part of fluid models used to describe SOL turbulence [24]. The rationale for this conjecture stems from the extrapolation to infinite dimensions of the mathematical findings that finite-dimensional vector fields are always decomposable into Hamiltonian (conservative) plus gradient (dissipative) components, and that what often occurs is that the full system ends up depicting, in some regions of phase space, deformed versions of the Hamiltonian dynamics (hence the notion of constants of motion in dissipative systems) [25, 26].

To describe plasma dynamics in the SOL, more precisely, to evolve (in the cold-ion limit) its logarithmic density Ln and vorticity $\nabla^2\phi$, a simple two-dimensional, two-field fluid model has been used, which reads

$$
\begin{aligned}
\frac{\partial Ln}{\partial t} = & -[\phi, Ln] - g\partial_2(Ln - \phi) \\
& + D\left(\nabla^2 Ln + |\nabla Ln|^2\right) - \sigma_{\parallel}e^{(\Lambda - \phi)} + S \\
\frac{\partial \nabla^2\phi}{\partial t} = & -[\phi, \nabla^2\phi] - g\partial_2 Ln + \nu\nabla^4\phi + \sigma_{\parallel}\left[1 - e^{(\Lambda - \phi)}\right]
\end{aligned}
\tag{1}
$$

and can be found in the literature in identical or very similar forms [2, 4, 5, 27, 28]. In (1), Ln and ϕ are functions of time t and of the radial- and poloidal-like coordinates $x_1 = r - a$ and $x_2 = a\theta$, respectively (with a the minor radius of the core plasma), $g = \partial_1(1/B)$ is the curvature of the magnetic field $\mathbf{B}$ (taken to be independent of x_2 and such that $\widehat{\mathbf{b}} = \mathbf{B}/B = \nabla x_1 \times \nabla x_2$), D and ν are coefficients describing particle and vorticity diffusion, respectively, $\sigma_{\parallel}$ accounts for parallel (along the magnetic field) losses to the walls or limiters, Λ stands for the floating potential, whilst S represents a source of incoming plasma from the core, and properly normalised quantities are used throughout. In addition, $[u, v] = \partial_1 u\partial_2 v - \partial_2 u\partial_1 v = \widehat{\mathbf{b}} \cdot \nabla u \times \nabla v$ denotes the canonical Poisson bracket, $\nabla = (\partial_1, \partial_2)$ is the standard del operator and $\partial_i = \partial/\partial x_i$. The conservative part of model (1) is that which is constructed solely with Poisson brackets and governs convective transport in the perpendicular (to the magnetic field) direction [29], so

$$
\begin{aligned}
\frac{\partial Ln}{\partial t} = & -[\phi, Ln] - g\partial_2(Ln - \phi) \\
\frac{\partial \nabla^2\phi}{\partial t} = & -[\phi, \nabla^2\phi] - g\partial_2 Ln,
\end{aligned}
\tag{2}
$$

section 2 of this paper being devoted to exploring solutions to (2) that mimic blob-like behaviour. More precisely, exact

travelling-wave-type solutions are shown for the conservative system (2) which correspond to large-scale, coherent structures moving concentrations of particles and energy across the plasma, radially and/or poloidally, some of which are conjectured to be the conservative ancestors of plasma blobs. After detailing the relation between the propagation velocity of these solutions and the $E \times B$ drift velocity in section 3, their usefulness for code verification, as they function as analytical standards against which numerical solutions can be benchmarked, is demonstrated in section 4. In section 5, numerical solutions of the complete model (1) are explored, aiming to ascertain, in particular, if the blob-like conservative solutions survive through the full dynamics. Finally, findings are discussed and conclusions drawn in section 6, with some derivations and numerical details (given here for the sake of completeness and pedagogy) being left for the appendices.

A few words should be said about the values chosen for the parameters entering models (1) and (2): they are in accordance with what has been reported in the literature addressing similar SOL models [1, 2, 4, 5, 27, 28], but have to be rescaled because of the different sizes of the simulation 'boxes' where these models are solved. In fact, suppose the set of parameters is imported from simulations carried out on a square 'box' of size $\Delta x_1 \times \Delta x_2 = L^2$ (simulations in this paper being set on a $\Delta x_1 \times \Delta x_2 = 1^2$ square 'box'), then all spatial dimensions in the imported quantities have to be rescaled according to $x_i \to x_i/L$, which implies that both the magnetic curvature and the parallel losses (which scale, respectively, as $g \sim R_0^{-1}$ and $\sigma_{\parallel} \sim L_{\parallel}^{-1} \sim R_0^{-1}$, with R_0 the tokamak major radius and $L_{\parallel}$ the parallel connection length [1, 2, 4, 5, 27, 28]), must be transformed as $g \to Lg$ and $\sigma_{\parallel} \to L\sigma_{\parallel}$, whereas for the diffusion coefficients, one must have $D \to D/L^2$ and $\nu \to \nu/L^2$. Therefore, importing the same set of parameters used in simulations where $L \approx 100$ [4, 5], one ends up with $g = 0.08$, $D = \nu = 1 \times 10^{-6}$ and $\sigma_{\parallel} = 0.02$ for the constants appearing in models (1) and (2) of this article. For completeness, one also has $\Lambda = 3.9$, $S_0 = 5 \times 10^{-4}$ and $\lambda = 0.1$, the latter two defining the source profile $S(x_1) = e^{-Ln}S_0 e^{-x_1^2/\lambda^2}$, where the source e-folding length has also been rescaled according to $\lambda \to \lambda/L$[1].

2. Analytical solutions for the conservative model

Hence, and for constant g, exact solutions to (2) have been derived which are of the travelling-wave type and take the form [24]

$$
\begin{aligned}
Ln(x_1, x_2, t) = & f[F(x_1 - v_1 t, x_2 - v_2 t)] - gx_1 \\
\phi(x_1, x_2, t) = & F(x_1 - v_1 t, x_2 - v_2 t) \\
& + v_2(x_1 - v_1 t) - v_1(x_2 - v_2 t) - gx_1,
\end{aligned}
\tag{3}
$$

---

[1] Note that the e^{-Ln} factor appearing in the expression for the source $S(x_1)$ is simply due to the fact that one is working here with the logarithmic density, and that the original source $S_0 e^{-x_1^2/\lambda^2}$ is not taken proportional to plasma density [1, 2, 4, 5, 27, 28].
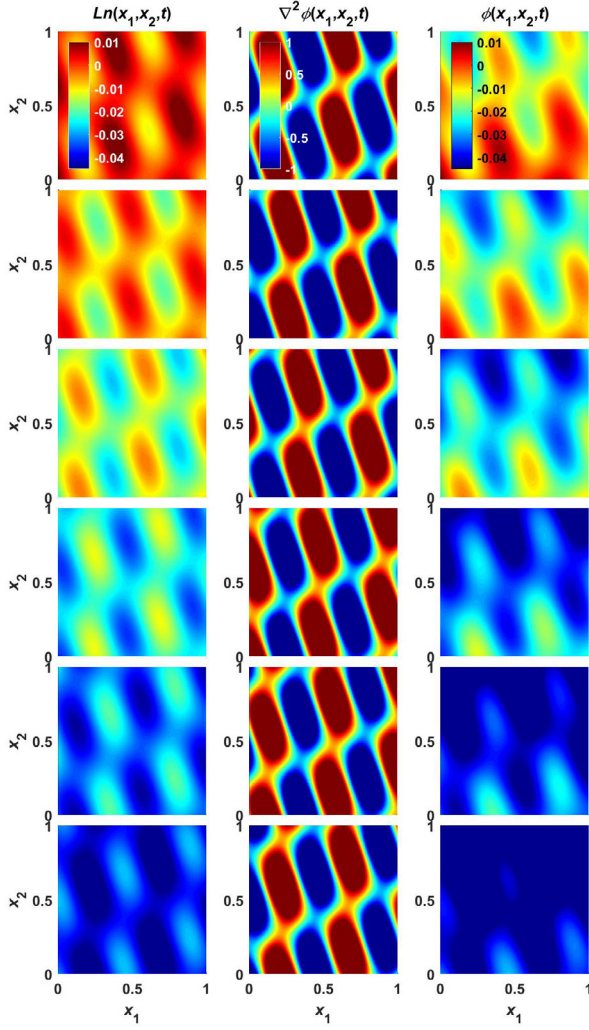
Figure 1. Snapshots with contour plots of the analytical logarithmic density $Ln(x_1, x_2, t)$, vorticity $\nabla^2\phi(x_1, x_2, t)$ and electrostatic potential $\phi(x_1, x_2, t)$ for solution (5), with $g = 0.08$, $\alpha = 1$, $B = C_0 = 0$, $A = C_1 = -C_2 = 0.005$, $k_1 = k_2 = 10$, $v_1 = 0.02$ and $v_2 = 0$.

Figure 2. Snapshots with contour plots of the analytical logarithmic density $Ln(x_1, x_2, t)$, vorticity $\nabla^2\phi(x_1, x_2, t)$ and electrostatic potential $\phi(x_1, x_2, t)$ for solution (6), with $g = 0.08$, $\alpha = 1$, $C_0 = 0$, $A = C_1 = C_2 = 0.1$, $k_1 = -0.5$, $k_2 = -0.1$, $v_1 = 0.025$ and $v_2 = 0.03$.

with f some arbitrary differentiable function and F obeying[2]

$$\partial_1 F \partial_2 \nabla^2 F - \partial_1 \nabla^2 F \partial_2 F + g\partial_2 \left[f(F) - \nabla^2 F \right] = 0. \quad (4)$$

Setting $f(F) = \alpha F$ and subsequently solving (4) leads to

$$
\begin{aligned}
Ln(x_1, x_2, t) = &\, \alpha \left[\phi(x_1, x_2, t) - v_2(x_1 - v_1 t) + v_1(x_2 - v_2 t) \right] \\
&+ (\alpha - 1) g x_1 \\
\phi(x_1, x_2, t) = &\left(v_2 + g + \frac{\alpha g}{k^2} \right)(x_1 - v_1 t) - v_1(x_2 - v_2 t) \\
&- g x_1 + A \cos\left[k_1(x_1 - v_1 t) + k_2(x_2 - v_2 t) \right] \\
&+ B \sin\left[k_1(x_1 - v_1 t) + k_2(x_2 - v_2 t) \right] \\
&+ C_0 + C_1 \cos\left[k(x_1 - v_1 t) \right] \\
&+ C_2 \sin\left[k(x_1 - v_1 t) \right],
\end{aligned} \quad (5)
$$

or to

---

[2] Note that the solutions here obtained are not pure travelling waves due to the isolated gx_1 term in them, hence the denomination travelling-wave-type, or travelling-wave-like, solutions.
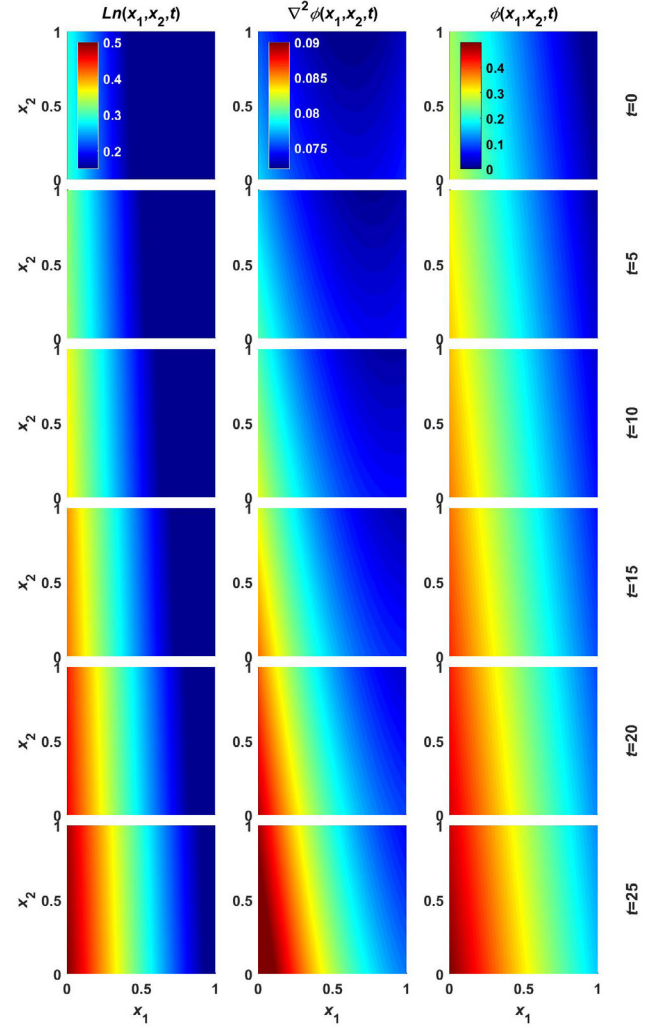
$$
\begin{aligned}
Ln(x_1, x_2, t) = &\, \alpha \left[\phi(x_1, x_2, t) - v_2(x_1 - v_1 t) + v_1(x_2 - v_2 t) \right] \\
&+ (\alpha - 1) g x_1 \\
\phi(x_1, x_2, t) = &\left(v_2 + g - \frac{\alpha g}{k^2} \right)(x_1 - v_1 t) - v_1(x_2 - v_2 t) - g x_1 \\
&+ A \exp\{[k_1(x_1 - v_1 t) + k_2(x_2 - v_2 t)]\} \\
&+ C_0 + C_1 \exp[k(x_1 - v_1 t)] + C_2 \exp[-k(x_1 - v_1 t)],
\end{aligned} \quad (6)
$$

where α, A, B, C_0, C_1 and C_2 are arbitrary constants, v_1 and v_2 are propagating velocities, and k_1 and k_2 are wave numbers, with $k^2 = k_1^2 + k_2^2$. Particular instances of (5) and (6) are plotted in figures 1 and 2, which depict the outward propagation of large-scale density and potential structures that complement those that have been previously reported [24], and illustrate the wide variety of exact solutions one may extract from the conservative part of SOL turbulence models, many of which are still waiting to be explored.
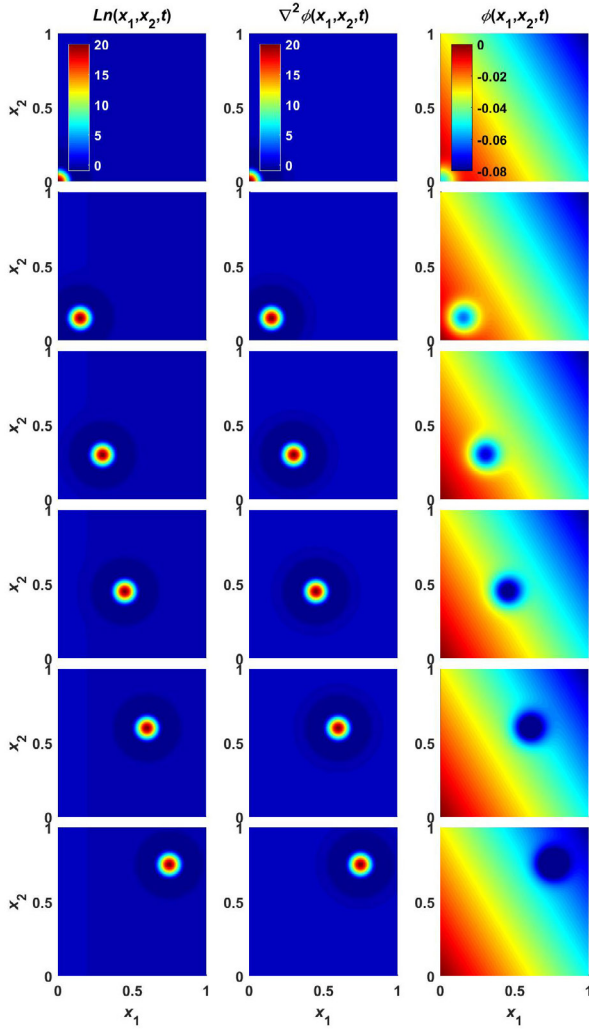
Figure 3. Snapshots with contour plots of the analytical logarithmic density $Ln(x_1, x_2, t)$, vorticity $\nabla^2 \phi(x_1, x_2, t)$ and electrostatic potential $\phi(x_1, x_2, t)$ for solution (11), with $g = 0.08$, $N = 1$, $A_1 = -0.05$, $\gamma_1 = 200$, $c_{10} = 0$ and $v_1 = v_2 = 0.03$.
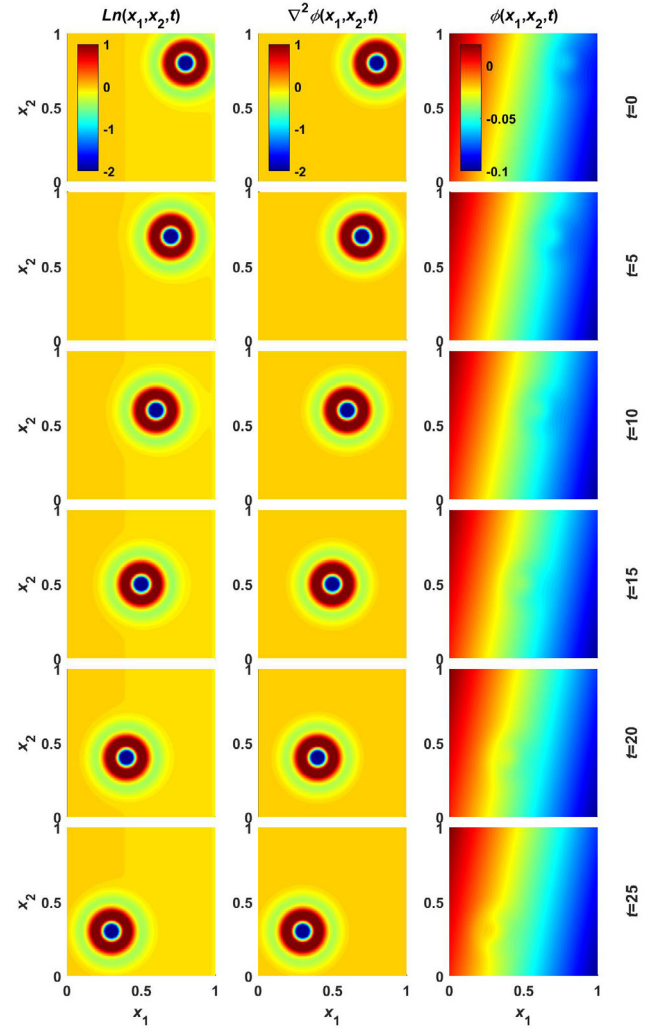
Figure 4. Snapshots with contour plots of the analytical logarithmic density $Ln(x_1, x_2, t)$, vorticity $\nabla^2 \phi(x_1, x_2, t)$ and electrostatic potential $\phi(x_1, x_2, t)$ for solution (12), with $g = 0.08$, $A = -1$, $\gamma = 180$, $c_0 = 0.8$ and $v_1 = v_2 = -0.02$.

In contrast to the previous extended solutions are the solutions of the form [24]

$$
Ln(x_1, x_2, t) = \nabla^2 F_s(x_1 - v_1 t, x_2 - v_2 t) - g x_1
$$
$$
\phi(x_1, x_2, t) = F_s(x_1 - v_1 t, x_2 - v_2 t)
$$
$$
+ v_2(x_1 - v_1 t) - v_1(x_2 - v_2 t) - g x_1,
$$
(7)

which allow for highly localised, Gaussian-shaped structures and where F_s is any symmetric function of its two arguments, meaning

$$
F_s(x_2 - v_2 t, x_1 - v_1 t) = F_s(x_1 - v_1 t, x_2 - v_2 t). \quad (8)
$$

It can be noted that (7) and (8) become a particular case of (3) and (4) if one makes $f(F) = \nabla^2 F$ and $F = F_s$. As an example, take the multi-Gaussian solution

$$
F_s(x_1, x_2, t) =
$$
$$
\sum_{i=1}^{N} A_i \exp\left\{ -(\gamma_i/2) \left[(x_1 - v_1 t - c_{i0})^2 + (x_2 - v_2 t - c_{i0})^2 \right] \right\},
$$
(9)

or the sinusoidally modulated Gaussian

$$
F_s(x_1, x_2, t) =
$$
$$
A \sin\left[(x_1 - v_1 t - c_0)^2 + (x_2 - v_2 t - c_0)^2 \right]
$$
$$
\times \exp\left\{ -(\gamma/2) \left[(x_1 - v_1 t - c_0)^2 + (x_2 - v_2 t - c_0)^2 \right] \right\},
$$
(10)

which yield, respectively,

$$
Ln(x_1, x_2, t) =
$$
$$
- \sum_{i=1}^{N} A_i \gamma_i \left\{ 2 - \gamma_i \left[(x_1 - v_1 t - c_{i0})^2 + (x_2 - v_2 t - c_{i0})^2 \right] \right\}
$$
$$
\times \exp\left\{ -(\gamma_i/2) \left[(x_1 - v_1 t - c_{i0})^2 + (x_2 - v_2 t - c_{i0})^2 \right] \right\} - g x_1
$$
$$
\phi(x_1, x_2, t) =
$$
$$
\sum_{i=1}^{N} A_i \exp\left\{ -(\gamma_i/2) \left[(x_1 - v_1 t - c_{i0})^2 + (x_2 - v_2 t - c_{i0})^2 \right] \right\}
$$
$$
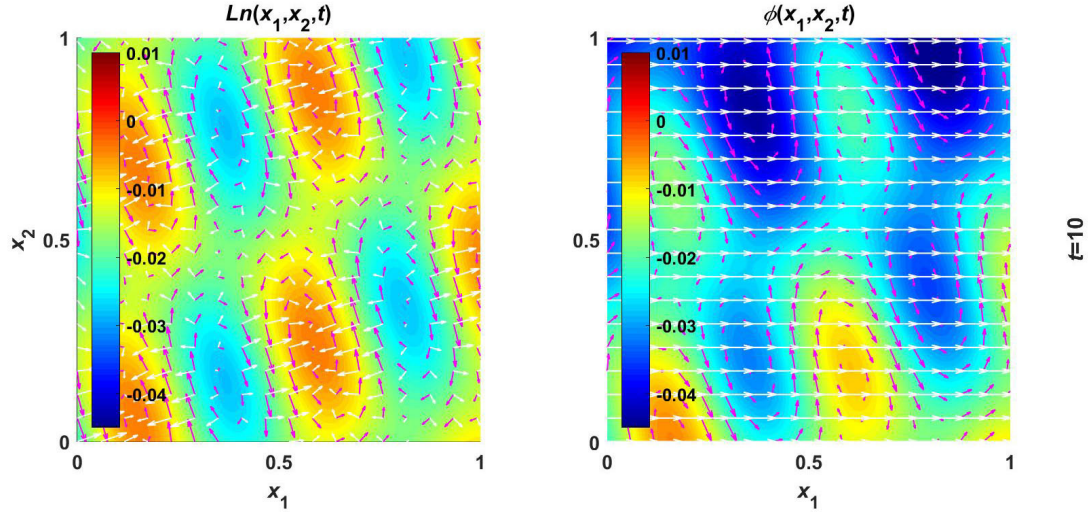+ v_2(x_1 - v_1 t) - v_1(x_2 - v_2 t) - g x_1,
$$
(11)

Figure 5. Snapshot of vector-field maps for the density gradient $\nabla Ln(x_1, x_2, t)$ and velocity difference $\mathbf{v}(x_1, x_2, t) - \mathbf{v}_{E \times B}(x_1, x_2, t)$ (respectively, white and magenta arrows on the left frame) and for the travelling and $E \times B$ velocities $\mathbf{v}(x_1, x_2, t)$ and $\mathbf{v}_{E \times B}(x_1, x_2, t)$ (respectively, white and magenta arrows on the right frame) for the analytical solution plotted in figure 1.

Figure 6. Snapshot of vector-field maps for the density gradient $\nabla Ln(x_1, x_2, t)$ and velocity difference $\mathbf{v}(x_1, x_2, t) - \mathbf{v}_{E \times B}(x_1, x_2, t)$ (respectively, white and magenta arrows on the left frame) and for the travelling and $E \times B$ velocities $\mathbf{v}(x_1, x_2, t)$ and $\mathbf{v}_{E \times B}(x_1, x_2, t)$ (respectively, white and magenta arrows on the right frame) for the analytical solution plotted in figure 3.
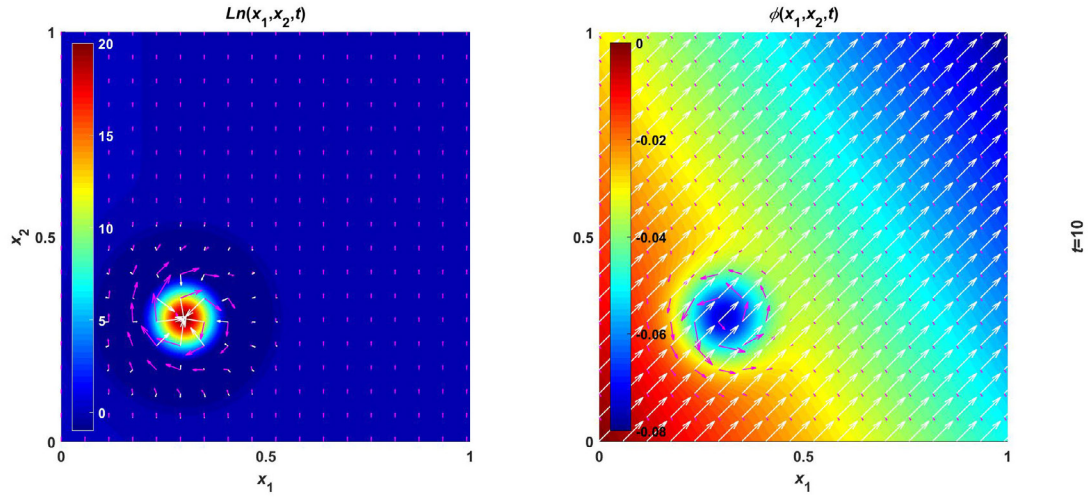
or

$$
\begin{aligned}
Ln\,(x_1, x_2, t) =\ & A\Big(4\Big\{1 - \gamma\Big[(x_1 - v_1 t - c_0)^2 + (x_2 - v_2 t - c_0)^2\Big]\Big\} \\
& \times \cos\Big[(x_1 - v_1 t - c_0)^2 + (x_2 - v_2 t - c_0)^2\Big] \\
& - \Big\{2\gamma + (4 - \gamma^2)\Big[(x_1 - v_1 t - c_0)^2 + (x_2 - v_2 t - c_0)^2\Big]\Big\} \\
& \times \sin\Big[(x_1 - v_1 t - c_0)^2 + (x_2 - v_2 t - c_0)^2\Big]\Big) \\
& \times \exp\Big\{-(\gamma/2)\Big[(x_1 - v_1 t - c_0)^2 + (x_2 - v_2 t - c_0)^2\Big]\Big\} - gx_1 \\
\phi\,(x_1, x_2, t) =\ & A\sin\Big[(x_1 - v_1 t - c_0)^2 + (x_2 - v_2 t - c_0)^2\Big] \\
& \times \exp\Big\{-(\gamma/2)\Big[(x_1 - v_1 t - c_0)^2 + (x_2 - v_2 t - c_0)^2\Big]\Big\} \\
& + v_2\,(x_1 - v_1 t) - v_1\,(x_2 - v_2 t) - gx_1.
\end{aligned}
\tag{12}
$$

Appropriate choices of γ and γ_i, which set the widths of the Gaussians, and of c_0 and c_{i0}, which determine their initial locations, lead to the cases shown in figures 3 and 4. These are particularly striking as they demonstrate that the conservative solutions studied here are not only able to reproduce outwardly moving plasma blobs, but can also mimic inwardly moving plasma holes (whose density is smaller than that of the background) [13, 16, 23]. It must be kept in mind that many of the conservative solutions given hereabove (say, for instance, the solutions depicted in figures 1 and 2) may not be representative of what one expects regarding blob physics in the SOL of fusion devices. Solutions such as (5), (6), (11) and (12) are indeed exact solutions of the conservative interchange model (2), but they live in unbounded space and exist for all time, not being restricted to emerging and existing in a limited box (where, given an initial condition, computations are made and boundary conditions imposed).
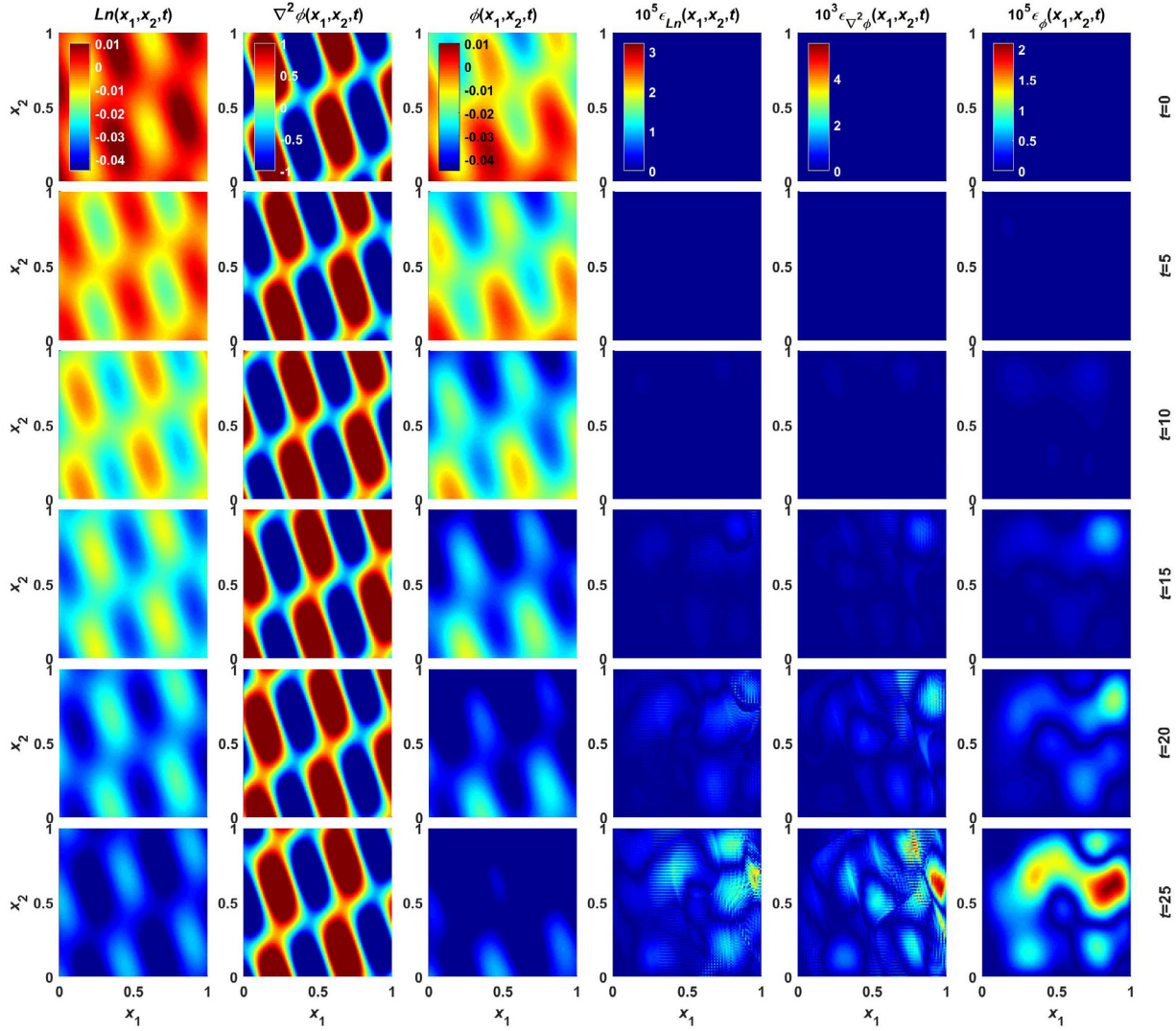
Figure 7. Snapshots with contour plots of the numerical logarithmic density $Ln(x_1, x_2, t)$, vorticity $\nabla^2 \phi(x_1, x_2, t)$ and electrostatic potential $\phi(x_1, x_2, t)$, and of their respective local errors $\epsilon_{Ln}(x_1, x_2, t)$, $\epsilon_{\nabla^2 \phi}(x_1, x_2, t)$ and $\epsilon_\phi(x_1, x_2, t)$, for $N_1 = N_2 = 101$ and $\Delta t = 10^{-2}$, and for the same set of parameters and initial condition as the analytical solution plotted in figure 1.

3. $E \times B$ drift versus travelling velocity

The travelling-wave-like solutions depicted above propagate with constant, pre-defined and independently set velocities $\mathbf{v} = (v_1, v_2)$, yet one should expect density structures in a plasma to be transported by means of the $E \times B$ drift, that is, with a velocity $\mathbf{v}_{E \times B} = \mathbf{E} \times \widehat{\mathbf{b}} = -\nabla \phi \times \widehat{\mathbf{b}} = (-\partial_2 \phi, \partial_1 \phi)$ (assuming a normalised magnetic field whose amplitude variation across the SOL has a negligible impact on $\mathbf{v}_{E \times B}$), which gives an advective contribution $\mathbf{v}_{E \times B} \cdot \nabla u$ to the total time derivative of some plasma quantity u [1–19, 21–23, 28–30]. In fact, $E \times B$ advection is indeed included in the model equations (1) and (2), namely, in the first term on their right-hand sides (rhs's), since $\mathbf{v}_{E \times B} \cdot \nabla u = \widehat{\mathbf{b}} \times \nabla \phi \cdot \nabla u = \widehat{\mathbf{b}} \cdot \nabla \phi \times \nabla u = [\phi, u]$, and so density as well as, for that matter, vorticity are locally transported with a velocity $\mathbf{v}_{E \times B}$. Needless to say, being exact solutions of the model, density is indeed *locally* advected with

$E \times B$ velocity $\mathbf{v}_{E \times B}$ in figures 1–4, even if *global* structures travel with velocity $\mathbf{v}$. With the help of (3), the relation

$$\mathbf{v} = \mathbf{v}_{E \times B} + (\partial_2 F, g - \partial_1 F) \qquad (13)$$

follows between the two velocities, its projection in the direction of the density gradient reading

$$\nabla Ln \cdot (\mathbf{v} - \mathbf{v}_{E \times B}) = [f(F), F] + g \partial_2 [f(F) - F] \quad (14)$$

or, considering that both $[f(F), F] = f'(F)[F, F] = 0$ and $[\nabla^2 F_s, F_s] = 0$,

$$\nabla Ln \cdot (\mathbf{v} - \mathbf{v}_{E \times B}) = g \partial_2 [f(F) - F] \qquad (15)$$

or, still,

$$\nabla Ln \cdot (\mathbf{v} - \mathbf{v}_{E \times B}) = g [\partial_2 (Ln - \phi) - v_1]. \qquad (16)$$

The fact that $\mathbf{v}$ and $\mathbf{v}_{E \times B}$ are not identical thus causes no contradiction at all, the actual restriction linking the two being conveyed by (13), (15) or (16), the two latter conditions being easier to understand when their rhs's vanish. In the particular
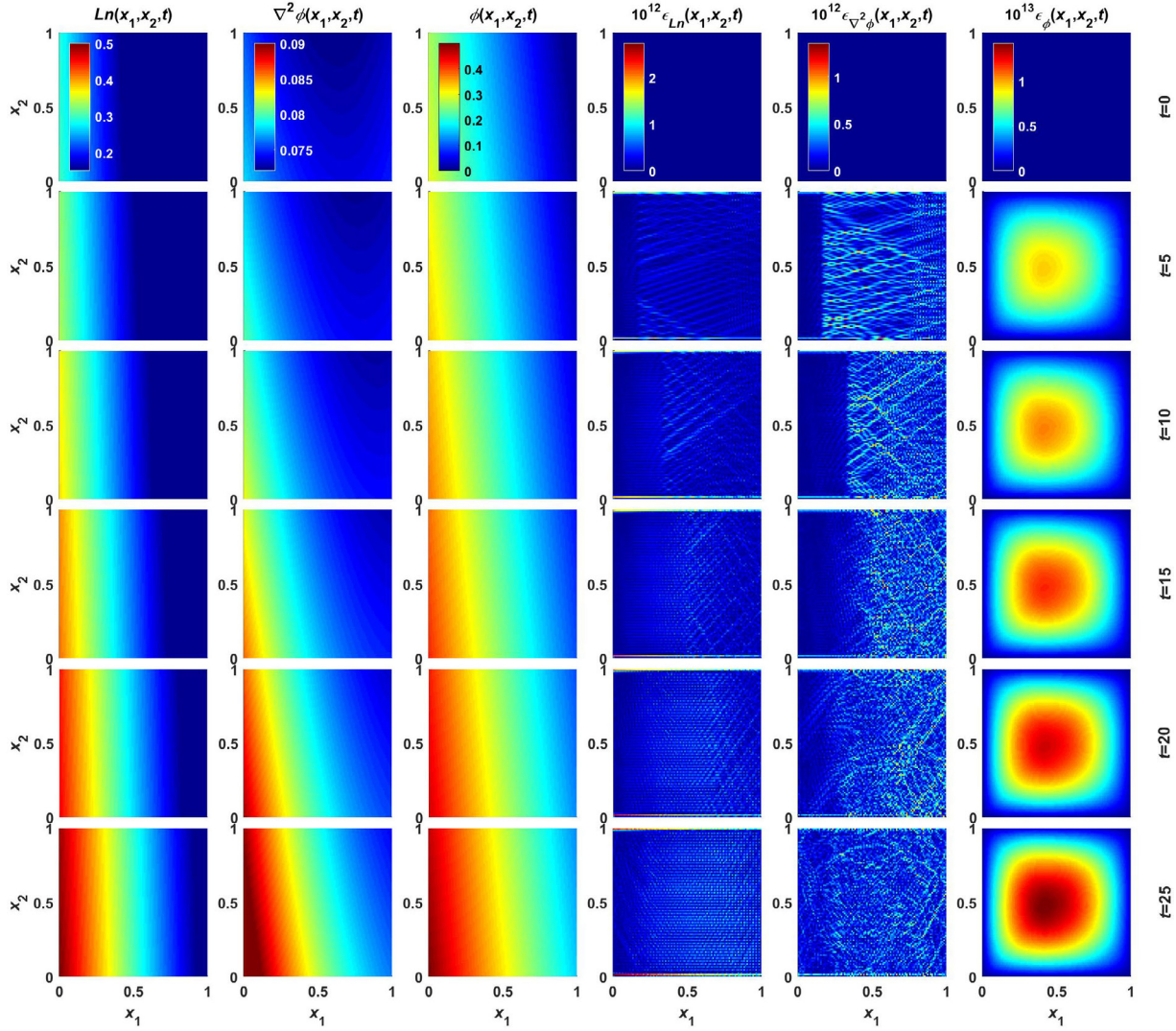
Figure 8. Snapshots with contour plots of the numerical logarithmic density $Ln(x_1, x_2, t)$, vorticity $\nabla^2\phi(x_1, x_2, t)$ and electrostatic potential $\phi(x_1, x_2, t)$, and of their respective local errors $\epsilon_{Ln}(x_1, x_2, t)$, $\epsilon_{\nabla^2\phi}(x_1, x_2, t)$ and $\epsilon_\phi(x_1, x_2, t)$, for $N_1 = N_2 = 101$ and $\Delta t = 10^{-2}$, and for the same set of parameters and initial condition as the analytical solution plotted in figure 2.

case for which $g = 0$, (2) simply states that Ln and $\nabla^2\phi$ are conserved quantities as they are moved with velocity $\mathbf{v}_{E\times B}$ along the $E \times B$ flow, while simultaneously (3) and (7) become pure travelling-wave solutions transporting those two quantities with velocity $\mathbf{v}$.

For instance, when $f(F) = \alpha F$ and $\alpha = 1$, which is the case for solutions plotted in figures 1 and 2, the rhs of (15) is zero and so $\mathbf{v} - \mathbf{v}_{E\times B}$ must be perpendicular to ∇Ln, which means the two velocities $\mathbf{v}$ and $\mathbf{v}_{E\times B}$ need not be equal but only their projections in the direction of the density gradient. This is illustrated in figure 5, where it can be verified that $\mathbf{v} - \mathbf{v}_{E\times B}$ and ∇Ln are indeed perpendicular to each other and, moreover, that $\mathbf{v}_{E\times B}$ (clearly distinct fom $\mathbf{v}$) follows the lines of constant ϕ (the equipotentials), as it should, given that it is, by definition, perpendicular to $\nabla\phi$. Replacing $f(F)$ with $\nabla^2 F_s$ on the rhs of (15), the latter is no longer strictly zero, but may be negligible depending on the smallness of g, as can be observed in figure 6. In fact, note that for F_s given by (9), which leads to solution (11) and the plots in figure 3, follows (with $N_1 = 1$ and $c_{10} = 0$)

$$\partial_2 \left(\nabla^2 F_s - F_s\right) = \left\{\gamma_1 + 4\gamma_1^2 - \gamma_1^3 \left[(x_1 - v_1 t)^2 + (x_2 - v_2 t)^2\right]\right\} (x_2 - v_2 t) F_s, \tag{17}$$

whose rhs is seen to approach zero both when moving nearer the blob center and when moving further away from it (since one has either $\gamma_1^{1/2}|x_2 - v_2 t| \ll 1$ or $\gamma_1^{1/2}|x_2 - v_2 t| \gg 1$, respectively). In the intermediate region (where $\gamma_1^{1/2}|x_1 - v_1 t| \approx \gamma_1^{1/2}|x_2 - v_2 t| \approx 1$) one has $\left|\partial_2 \left(\nabla^2 F_s - F_s\right)\right| \approx 2\gamma_1^{3/2}|F_s|$ if $\gamma_1 \gg 1$, hence $\left|g\partial_2 \left(\nabla^2 F_s - F_s\right)\right| \lesssim 2g\gamma_1^{3/2}|A_1| \approx 23$, and one can see in figure 6 that $\mathbf{v} - \mathbf{v}_{E\times B}$ and ∇Ln are indeed not perpendicular in this region and moreover that, with such a reasonably large g and accounting for (7), (9) and (13), $\mathbf{v}_{E\times B} \approx (v_1, v_2 - g)$ and $\mathbf{v} - \mathbf{v}_{E\times B} \approx (0, g)$ in the far region[3].

---

[3] Note that different vector fields in figures 5 and 6 (such as $\mathbf{v}$ and $\mathbf{v}_{E\times B}$ on their right frames) are plotted using different scales, so length ratios do not, in general, translate into actual ratios for vectors that do not belong to the same mapped field.
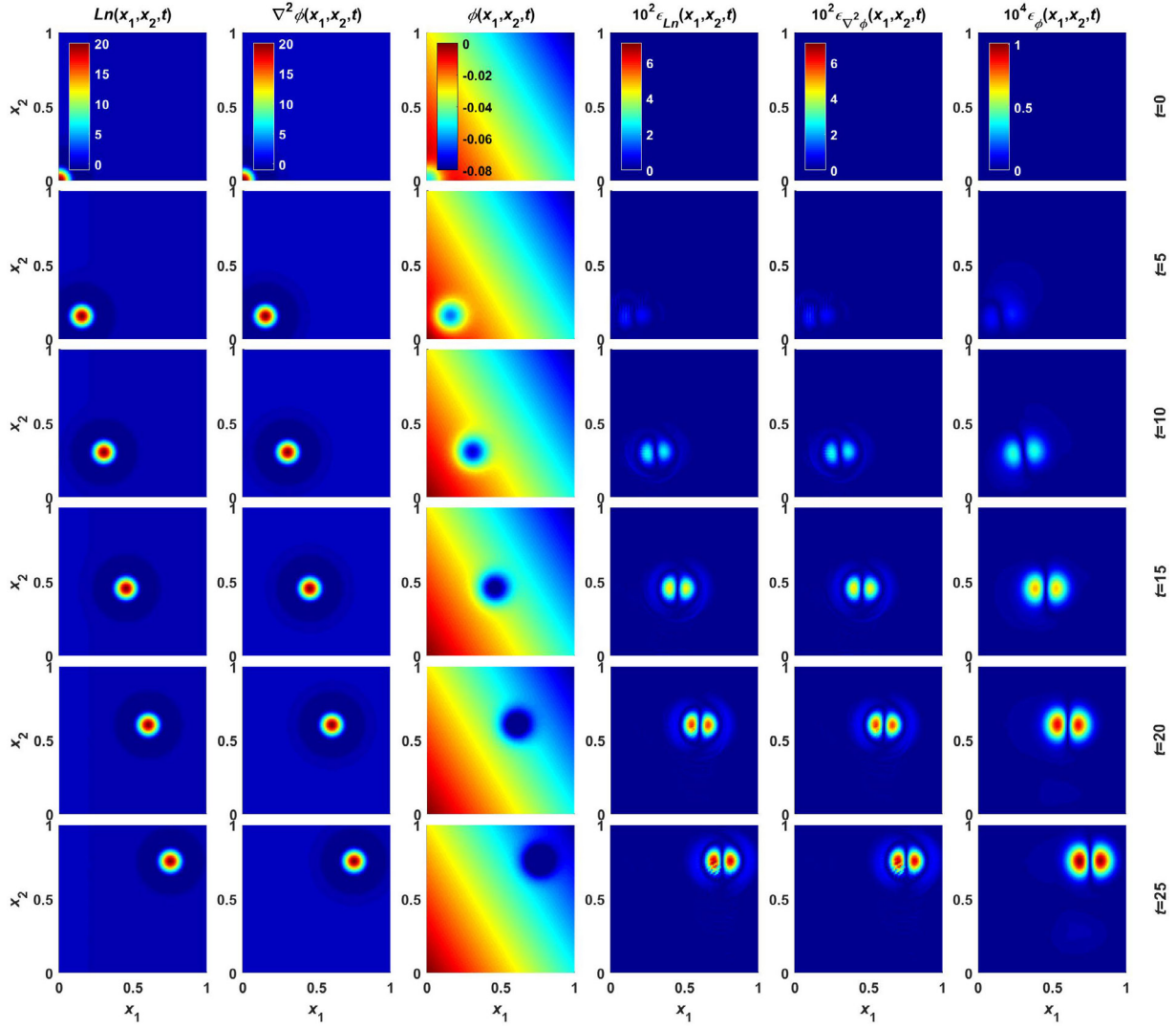
Figure 9. Snapshots with contour plots of the numerical logarithmic density $Ln\,(x_1, x_2, t)$, vorticity $\nabla^2\phi\,(x_1, x_2, t)$ and electrostatic potential $\phi\,(x_1, x_2, t)$, and of their respective local errors $\epsilon_{Ln}\,(x_1, x_2, t)$, $\epsilon_{\nabla^2\phi}\,(x_1, x_2, t)$ and $\epsilon_\phi\,(x_1, x_2, t)$, for $N_1 = N_2 = 101$ and $\Delta t = 10^{-2}$, and for the same set of parameters and initial condition as the analytical solution plotted in figure 3.

4. Analytical solutions as benchmarks for code verification

Besides the importance and added value that solutions (5), (6), (11) and (12) have *per se*, as they are actual solutions of the conservative part of the interchange model, they also allow some measure of analytical control over numerical implementations of the model as they provide benchmarks, or standards, against which these latter can be verified and gauged, being worthy to emphasise they are true (as opposed to manufactured [19, 31]) solutions. Therefore, to solve (1), a fourth order (in time) Runge–Kutta (RK4) scheme (with spatial derivatives computed making use of fourth order central finite differences) has been implemented [32], and has been verified by numerically solving (2) and comparing with the exact analytical solutions obtained. Leaving the numerical details for appendix B, it is nonetheless worth noting here that, in carrying out this verification procedure, the implementation of boundary conditions is not trivial and must be dealt with with extra care, as the latter are not static but evolve in time (being

provided by the analytical solutions, which extend throughout the entire space and are not limited to the integration domain). More precisely, when going through the intermediate time steps of the implemented RK4 scheme [32], boundary conditions must be sampled from the analytical solutions at precisely the same times at which the time derivatives appearing on the lhs's of (2) are evaluated.

So, numerical solutions to the conservative model (2) have been obtained having recourse to an RK4 solver, using an $N_1 \times N_2$ grid equally spaced in $x_1 \times x_2$ and a time step Δt, and quantifying the local error in the numerical estimate $u_{\mathrm{num}}(x_1, x_2, t)$ of some model field quantity $u(x_1, x_2, t)$ resulting from discretising (2) as

$$\epsilon_u(x_1, x_2, t) = |u_{\mathrm{num}}(x_1, x_2, t) - u(x_1, x_2, t)|, \qquad (18)$$

with $u(x_1, x_2, t)$ in (18) the value given by the analytical solution and starting with the initial condition $u_{\mathrm{num}}(x_1, x_2, 0) = u(x_1, x_2, 0)$. The comparison between the analytical solutions and their numerical counterpart is shown in figures 7–10, where one can see that there is no visible
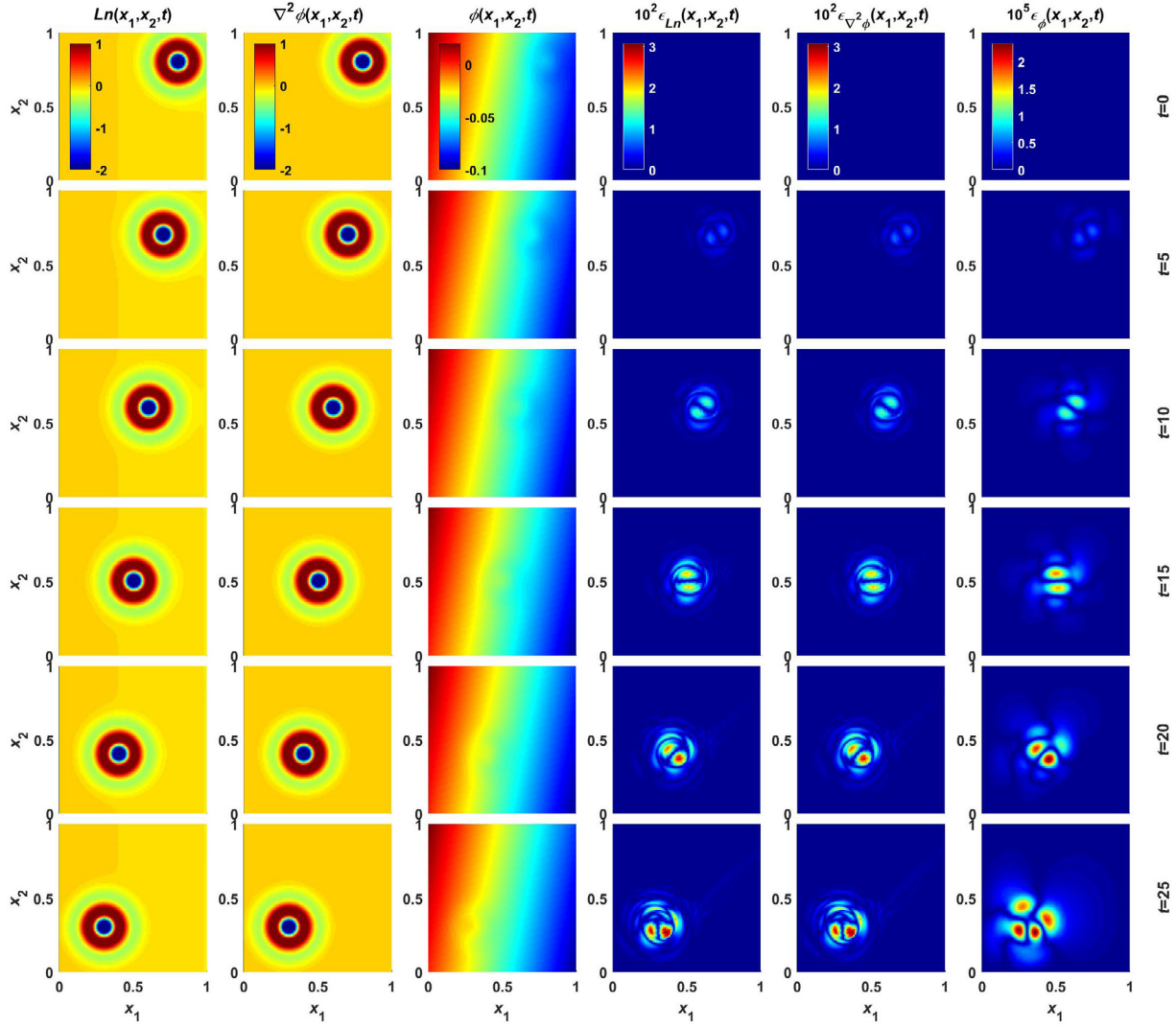
Figure 10. Snapshots with contour plots of the numerical logarithmic density $Ln(x_1, x_2, t)$, vorticity $\nabla^2\phi(x_1, x_2, t)$ and electrostatic potential $\phi(x_1, x_2, t)$, and of their respective local errors $\epsilon_{Ln}(x_1, x_2, t)$, $\epsilon_{\nabla^2\phi}(x_1, x_2, t)$ and $\epsilon_\phi(x_1, x_2, t)$, for $N_1 = N_2 = 101$ and $\Delta t = 10^{-2}$, and for the same set of parameters and initial condition as the analytical solution plotted in figure 4.

difference between the solutions in these plots and those in figures 1–4, and, further, that the local error-field values are comfortably within acceptable values. In general, albeit more apparent in the extended solutions of figures 7 and 8 than in the more localised, blob-like solutions of figures 9 and 10, the error patterns for ϵ_{Ln} and $\epsilon_{\nabla^2\phi}$ tend to remain more localised than for ϵ_ϕ, which can be explained by the fact that the logarithmic density Ln and vorticity $\nabla^2\phi$ are governed by the two very similar equations in (2) (which are numerically solved via an RK4 scheme involving only the closest neighbouring points in the grid), whereas the potential ϕ is calculated by inverting Poisson's equation (which is done via a matrix inversion or elimination operation that ends up involving all points in the grid). Global relative errors have also been defined according to [33, 34]

$$\varepsilon_u(t) = \frac{\sum_{i=0}^{N_1} \sum_{j=0}^{N_2} \epsilon_u(i/N_1, j/N_2, t)}{\sum_{i=0}^{N_1} \sum_{j=0}^{N_2} |u(i/N_1, j/N_2, t)|}, \qquad (19)$$

which remain safely below 8×10^{-3}, as can be verified in figure 11, where one also sees that, for most of them and

very much as expected, the errors in the numerical solutions grow linearly with time, but for the very first iterates, in which case the pronounced, almost instantaneous increase is a consequence of the very small initial error (when the analytical and numerical solutions are basically coincident). A possible exception to the linear growth of the global errors are the red curves in figure 11 (corresponding to the solution in figure 7), which can be viewed more as an exponential growth, the faster increase in the latter being probably linked to the fact that the density and potential structures become smaller and smaller, approaching more and more the scale of the computational grid and eventually leading to a loss of accuracy caused by numerical dissipation. Note, however, that this behaviour stems from the particulars of the solution plotted in figures 1 and 7, whose analytical form is given in (5) and for which one has the large time asymptotic limit $Ln \approx \alpha\phi \approx -\alpha g(1 + \alpha/k^2)v_1 t$ (so that, within the domain shown, the initial trigonometrically structured layout ends up being replaced by a uniform background whose absolute value grows indefinitely), and is not the result of some direct cascade from lower to higher wave numbers (or from larger to smaller structures), a context that is different
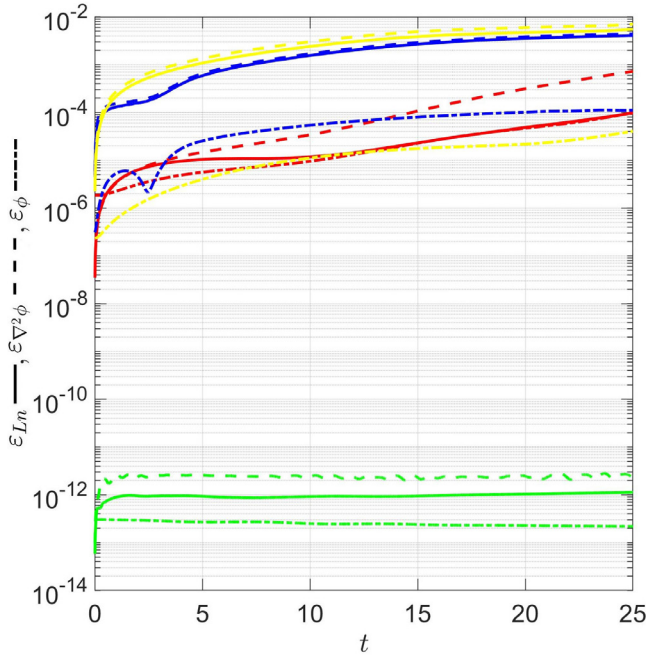
Figure 11. Global relative errors $\varepsilon_{Ln}(t)$, $\varepsilon_{\nabla^2\phi}(t)$ and $\varepsilon_\phi(t)$ for the numerical logarithmic density, vorticity and electrostatic potential plotted in figures 7 (red), 8 (green), 9 (blue) and 10 (yellow).

from that discussed below in connection with the complete model (1) depicted in figure 15[4]. That the numerical procedure converges to the expected order of accuracy, assumed to be 4 because both the time advancing and the finite differencing schemes are truncated at the fourth order, has been checked as well by conducting the test detailed in appendix C [31, 35].

5. Numerical solutions of the complete model

Having used the analytical conservative solutions to verify the implemented numerical algorithm, it is now possible to move forward and numerically explore the physics of the more complete SOL model (1), which will be done by gradually scaling up the starting, conservative model (2). Since one is no longer, say, running the analytical solutions, which called for the use of appropriate, time-evolving boundary conditions, a more realistic set will be used for the latter which, unless otherwise stated, is as follows: in the radial-like variable x_1 vorticity and potential will be set to zero at the boundaries, $\nabla^2\phi_{num}(-i/N_1, j/N_2, t) = \phi_{num}(-i/N_1, j/N_2, t) = \nabla^2\phi_{num}(1 + i/N_1, j/N_2, t) = \phi_{num}(1 + i/N_1, j/N_2, t) = 0$, and the logarithmic density will obey vanishing-derivative conditions, $Ln_{num}(-i/N_1, j/N_2, t) = Ln_{num}(i/N_1, j/N_2, t)$ and $Ln_{num}(1 + i/N_1, j/N_2, t) = Ln_{num}(1 - i/N_1, j/N_2, t)$, whereas in the poloidal-like variable x_2 periodic boundary conditions will apply for any of the three fields, $u_{num}(i/N_1, -j/N_2, t) = u_{num}(i/N_1, 1 - j/N_2, t)$ and $u_{num}(i/N_1, 1 + j/N_2, t) = u_{num}(i/N_1, j/N_2, t)$. In addition, and because the main interest is in blob dynamics,

---

[4] For a direct (or inverse) cascade to be observed, the underlying mechanism of the splitting (or merging) of turbulent eddies has to be present, which is obviously not the case with the travelling-wave-like conservative solutions discussed so far.
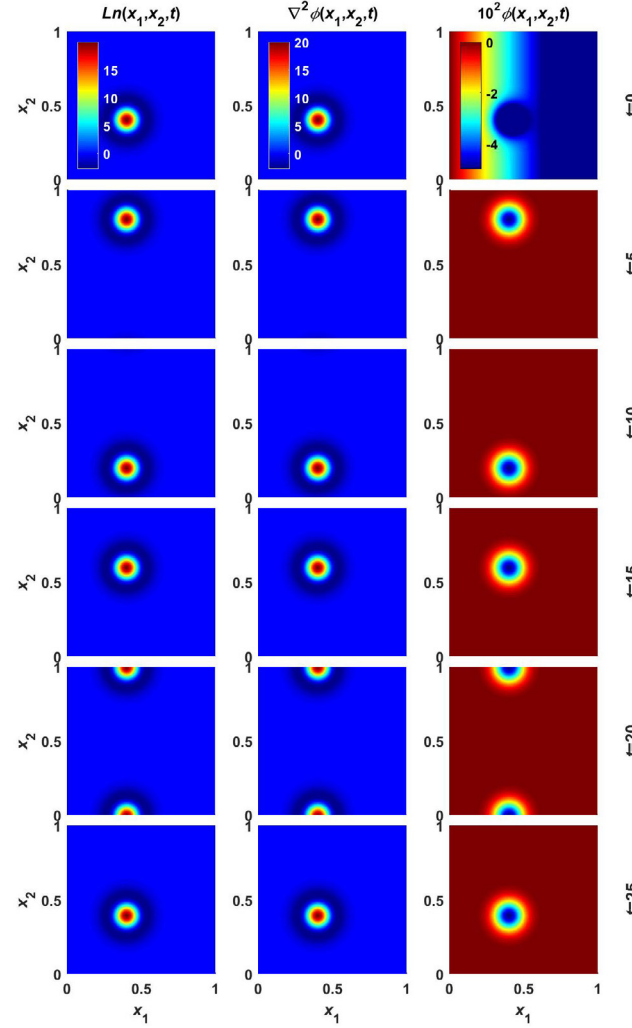

Figure 12. Snapshots with contour plots of the numerical logarithmic density $Ln(x_1, x_2, t)$, vorticity $\nabla^2\phi(x_1, x_2, t)$ and electrostatic potential $\phi(x_1, x_2, t)$, for $N_1 = N_2 = 201$ and $\Delta t = 10^{-2}$, and for model (2) with initial condition (11), and with $g = 0.08$, $N = 1$, $A_1 = -0.05$, $\gamma_1 = 200$, $c_{10} = 0.4$ and $v_1 = v_2 = 0$.

localised solutions of types (11) or (12) will henceforth be considered as initial conditions, which have the further advantage of possessing Gaussian-like shapes and thus providing appropriate natural seeds for seeded-blob simulations [2, 6, 9, 13–19], even more so as such seeds, being actual solutions of the conservative model, are self-justified.

The first runs consisted of simulating the conservative model (2) fully numerically, starting with initial conditions given by (11) or (12), two cases being shown in figures 12 and 13, where one should notice that the blob-like structures do move (essentially poloidally, without distortion and despite the fact that no travelling-wave velocity has been imposed) and are rendered periodic (under the effect of the periodic boundary conditions forced in the poloidal-like variable). The upward motion in x_2 of the blob-like structures can actually be explained in terms of an opposite, downward motion of the background driven by the $-gx_1$ term appearing in ϕ given in (11) and (12), which gives rise to a negative $\nabla\phi$ (clearly
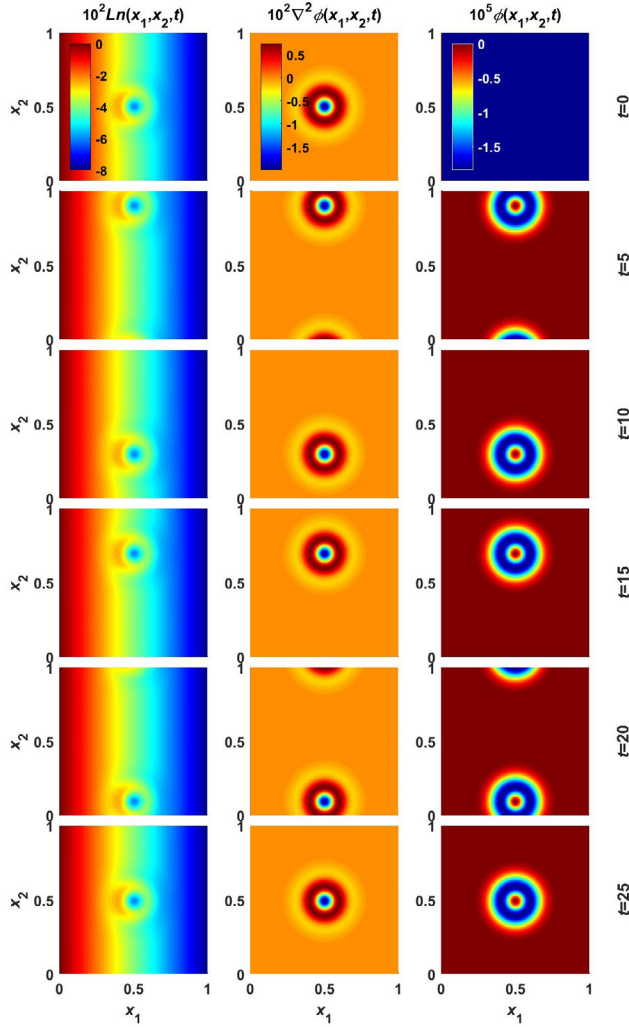
Figure 13. Snapshots with contour plots of the numerical logarithmic density $Ln(x_1, x_2, t)$, vorticity $\nabla^2\phi(x_1, x_2, t)$ and electrostatic potential $\phi(x_1, x_2, t)$, for $N_1 = N_2 = 201$ and $\Delta t = 10^{-2}$, and for model (2) with initial condition (12), and with $g = 0.08$, $A = -0.005$, $\gamma = 200$, $c_0 = 0.5$ and $v_1 = v_2 = 0$.

visible in the top, rightmost frames of figures 12, 14 and D1, albeit not in figures 13 and D2 because of the compressed scale) and a concomitant electric field $E = -\nabla\phi$ aligned along x_1 and pointing rightwards, whose interplay with the magnetic field pointing in the $\nabla x_1 \times \nabla x_2$ direction leads to the observed background $E \times B$ drift. As for the blob-like structure itself, take figure 12 for instance, the electric field points radially towards its centre, thus yielding an anticlockwise $E \times B$-induced spinning motion of the structure, something that can be confirmed by inspection of the right frame of figure 6. Examples with boundary conditions different from those detailed above have been used in relation to appendix D, where the conservative model is fully solved numerically and is put to use in situations where energy conservation is expected [29], in order to verify whether numerical dissipation has been kept under control.

To impart more physics to the model and thus proceed from (2) to (1), diffusive terms have been included that account for dissipation and essentially work as mimickers for perpendicular collisional transport and as numerical stabilisers
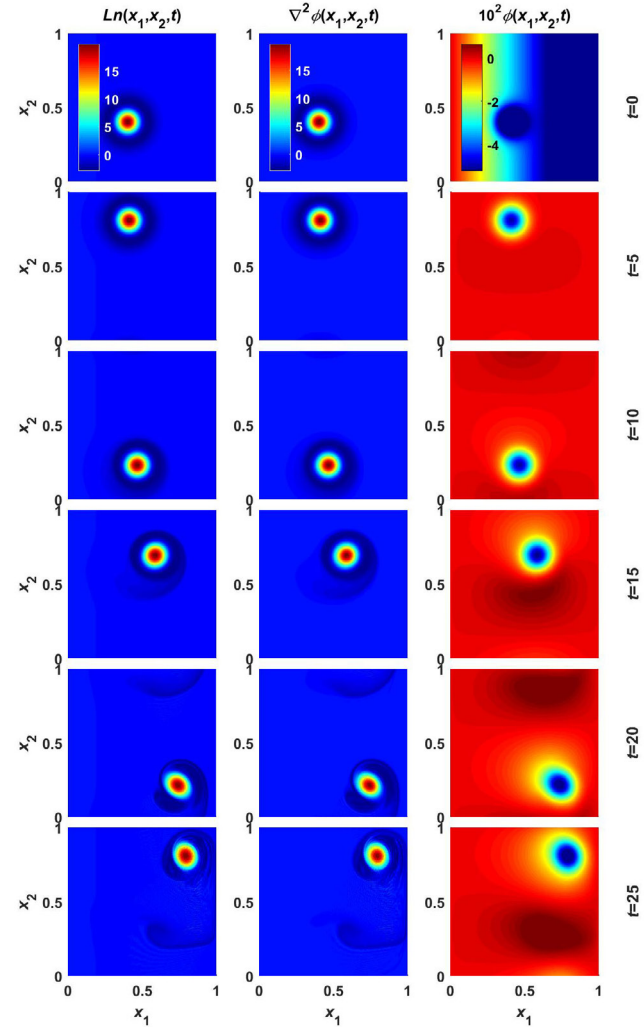
Figure 14. Snapshots with contour plots of the numerical logarithmic density $Ln(x_1, x_2, t)$, vorticity $\nabla^2\phi(x_1, x_2, t)$ and electrostatic potential $\phi(x_1, x_2, t)$, for $N_1 = N_2 = 201$ and $\Delta t = 10^{-2}$, and for model (1) with initial condition (11), and with $g = 0.08$, $D = \nu = 10^{-6}$, $N = 1$, $A_1 = -0.05$, $\gamma_1 = 200$, $c_{10} = 0.4$ and $v_1 = v_2 = 0$.

governing the decay of small structures [1–6, 15–19, 27, 28, 30, 31], the results of a run with these terms added being plotted in figure 14, where some distortion of the Gaussian-like initial condition takes place, along with the emergence of an outward radial motion. More precisely, dissipation combines with the anticlockwise spinning motion of the blob-like coherent structure to leave a trail that breaks the symmetry in the x_2 direction, thus creating along the latter a $\nabla\phi$ which, as seen in figure 14, is such as to give rise to an upward, x_2-aligned component of the E field, whose cross product with the $\nabla x_1 \times \nabla x_2$-aligned B field originates an $E \times B$ radially outward motion of the structure. Subsequently, the complete SOL model in (1) has been employed to obtain the outcome shown in figure 15, which very much resembles what can usually be found in the numerical and experimental literatures reporting on SOL turbulence and blobs [3–19, 28, 30]: a characteristic turbulent pattern sets in, on top of which a coherent structure (in the present case originating from the initial conservative condition) is transported, both radially
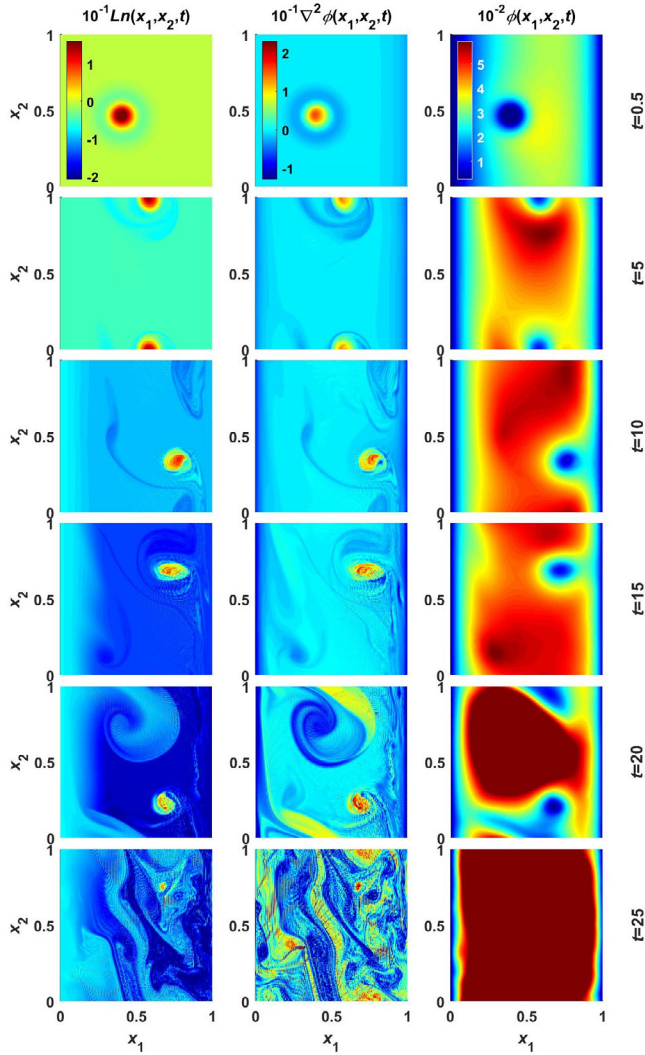
Figure 15. Snapshots with contour plots of the numerical logarithmic density $Ln(x_1, x_2, t)$, vorticity $\nabla^2\phi(x_1, x_2, t)$ and electrostatic potential $\phi(x_1, x_2, t)$, for $N_1 = N_2 = 201$ and $\Delta t = 10^{-3}$, and for model (1) with initial condition (11), and with $g = 0.08$, $D = \nu = 10^{-6}$, $\sigma_{||} = 0.02$, $\Lambda = 3.9$, $S_0 = 5 \times 10^{-4}$, $\lambda = 0.1$, $N = 1$, $A_1 = -0.05$, $\gamma_1 = 200$, $c_{10} = 0.4$ and $v_1 = v_2 = 0$.

and poloidally, surviving through most of the simulation and ending up by being eventually ejected or submerged in the turbulent background. Note, in addition, the development of narrow sheets in vorticity while the potential develops large-scale convective roll patterns that expand to the size of the computational box, indicating the formation of a dual cascade: direct (towards high wave numbers) in the case of vorticity and inverse (towards low wave numbers) in the case of potential. This simulation, where a coherent structure whose ancestor is an actual conservative solution behaves like a blob in every respect, goes towards supporting the initial conjecture according to which the solutions of the conservative part of the interchange model might be the ancestors of blobs.

6. Discussion and conclusions

In this paper, and complementing a previous analysis [24], exact travelling-wave-type solutions (travelling waves having

also been sought when addressing the origin of blobs following a different approach [23]) are shown for the conservative part (2) of a standard two-dimensional, two-fluid (density plus vorticity) model of the SOL (1) [2, 4, 5, 27, 28]. The aim has been to provide a more thorough exploration of such solutions and show once more that they possess the basic properties associated with blobs, namely, that they can describe convective, ballistic transport across the magnetic field of large, coherent structures in both directions (radial and poloidal) of the plasma cross-section. Based on known properties of dynamical systems [25, 26], a conjecture has been made that amongst these solutions might be the ancestors of blobs [24], the additional non-conservative terms (that account for diffusion, losses and sources) basically serving to distort the ballistic conservative dynamics. Moreover, it is interesting to note that some of these conservative solutions can take a Gaussian form, very much similar to the initial blobs (or holes) used in seeded simulations [2, 6, 9, 13–19], indicating such seed blobs may arise naturally from the conservative part of the equations, their use as initial conditions eventually helping to prevent (or reduce) large opening transients. The exact solutions here obtained have also been shown to play an important role as analytical benchmarks on which to verify and control the numerical implementation of the full model, a necessary step in testing the conjecture advanced above, and have been further checked regarding numerical dissipation and the order of accuracy of the numerical method.

Numerical solutions of the complete, non-conservative model have been explored with the aim of verifying, in particular, if the blob-like conservative solutions survive through most of the full dynamics (accounting for diffusion, parallel losses and sources), which has been indeed the case for the set of parameters tested. Although a more thorough and systematic analysis must be carried out (for instance, by sweeping the regions in parameter space where the physical quantities entering the equations take values that are relevant for present-day and future experiments), the results here reported apparently do not contradict the original conjecture that travelling-wave-like solutions of the conservative part of SOL turbulence models may indeed be the ancestors at the origin of blobs. Nonetheless, this is still at the stage of conjecture and should be interpreted in the sense that, if one feeds these conservative solutions to a standard interchange model of SOL turbulence, what emerges, and is shown in figure 15, is the characteristic picture of blob dynamics one sees in experiments and well-established simulations [3–19, 28, 30].

A further comment concerns the fact that the blob-like analytical conservative solutions derived here have a monopolar structure, as in figure 3, whereas it is well established as a model for blobs that a dipolar structure emerges as a consequence of charge separation brought about by curvature or ∇B drifts, which, in turn, creates an E field that combines with the ambient B field to produce the characteristic $E \times B$ outward radial motion [6, 9, 11–15, 20–22]. But this is precisely the sequence one observes as soon as the monopolar symmetry of the initial conservative solutions is broken, for instance by adding dissipation, as in figure 14. A possible reason why the dipolar structure does not emerge when numerically running the pure conservative model, as

in figures 12 and D1, is the rotational $E \times B$ motion created by the azimuthally symmetric potential (that creates a radial electric field within the structure), it being known that blob spinning tends to neutralise charge separation, thus reducing and eventually suppressing its radial motion [5, 9, 13–15]. Also, blobs with a net, strong monopolar structure are not physically irrelevant and play a role whenever there is a proportionality in the turbulent quantities between, on the one hand, the potential and, on the other, the density or the temperature (the former occurring when the blob electron density has a Maxwell–Boltzmann response and the potential becomes proportional to the logarithmic density, the latter when blobs are electrically connected to the sheaths and become subjected to a floating potential that scales linearly with temperature), since in both cases a radial profile (within the blob) develops for the potential, thus giving rise to a radial electric field and blob spinning [5, 9, 13–15]. Moreover, what becomes interesting in the present model as well (which has none of the physics just mentioned, that is, no Maxwell–Boltzmann electrons nor temperature-profile effects in connection with sheath phenomenology) is that its conservative solutions closely mimicking real blob behaviour have intrinsic net vorticity (or spin), which is not only important for understanding the formation of blobs with a strong monopolar structure, but (and this turns out to be even more interesting) it should also be confronted with the belief that, quite plausibly, blobs formed from turbulence are created already with a monopolar potencial (hence with intrinsic spin) [13].

Acknowledgments

Appendix A. Conservative model derivation

For the sake of pedagogy, the conservative set of equations (2) governing plasma advection in a poloidal-like plane $\nabla x_1 \times \nabla x_2$ perpendicular to the ambient magnetic field (oriented along $\widehat{\mathbf{b}} = \nabla x_1 \times \nabla x_2$) is now derived, starting from the equations that govern particles and charge conservation in a quasi-neutral plasma, respectively,

$$\frac{\partial n}{\partial t} + \nabla \cdot (n\mathbf{v}_e) = 0$$
$$\nabla \cdot [n(\mathbf{v}_i - \mathbf{v}_e)] = 0, \qquad (A.1)$$

where the electron velocity $\mathbf{v}_e = \mathbf{v}_{E \times B} + \mathbf{v}_{dia}$ is the sum of the $E \times B$ and diamagnetic drifts, whilst the ion velocity $\mathbf{v}_i = \mathbf{v}_{E \times B} + \mathbf{v}_{pol}$ adds up the $E \times B$ and polarisation drifts ($\mathbf{v}_{pol}$ being absent in $\mathbf{v}_e$ because electron inertia is negligible and $\mathbf{v}_{dia}$ not entering $\mathbf{v}_i$ because cold ions are assumed) [1, 6, 9, 12–14, 19–23, 28–30]. Recalling $\mathbf{v}_{E \times B} = \widehat{\mathbf{b}} \times \nabla \phi / B$, $\mathbf{v}_{dia} = -T_e \widehat{\mathbf{b}} \times \nabla Ln / eB$ (for isothermal electrons with temperature T_e and charge $-e$) and $\mathbf{v}_{pol} = -m_i (\partial/\partial t + \mathbf{v}_{E \times B} \cdot \nabla) \nabla \phi / eB^2$ (for cold ions with mass m_i and charge e), and after normalising B to some reference magnetic field B_0, n to the background density n_0, the electrostatic potential ϕ to the thermal energy per charge T_e/e, time t to the inverse of the ion cyclotron frequency $\Omega_i = eB_0/m_i$ and distances x_1 and x_2 to the ion Larmor radius $\rho_i = v_s/\Omega_i$ calculated using the ion sound speed $v_s = \sqrt{T_e/m_i}$, (A.1) becomes

$$\frac{\partial n}{\partial t} + \nabla \cdot \left[\frac{n\widehat{\mathbf{b}} \times \nabla(\phi - Ln)}{B} \right] = 0$$
$$\nabla \cdot \left\{ n \left[\frac{1}{B^2} \left(\frac{\partial}{\partial t} + \frac{\widehat{\mathbf{b}} \times \nabla \phi \cdot \nabla}{B} \right) \nabla \phi - \frac{\widehat{\mathbf{b}} \times \nabla Ln}{B} \right] \right\} = 0.$$
(A.2)

It is useful, in order to proceed, to identify those physical quantities that may be regarded as small and then formally introduce a small parameter δ to systematically expand the above equations. Therefore, with ϕ a perturbation and n and B taken as perturbations with respect to a reference, or background value, so $n = 1 + Ln + O(\delta^2)$ and $1/B = 1 + gx_1 + O(\delta^2)$, and being interested in the system's evolution at time scales much larger than $1/\Omega_i$, one sets $\partial/\partial t \sim \phi \sim Ln \sim g \sim \delta \ll 1$ [29]. This allows (A.2) to become

$$\frac{\partial Ln}{\partial t} + \nabla \left(Ln + \frac{1}{B} \right) \cdot \widehat{\mathbf{b}} \times \nabla(\phi - Ln)$$
$$+ \nabla \cdot \left[\widehat{\mathbf{b}} \times \nabla(\phi - Ln) \right] + O(\delta^3) = 0$$
$$\frac{\partial \nabla^2 \phi}{\partial t} + \nabla \cdot \left[\left(\widehat{\mathbf{b}} \times \nabla \phi \cdot \nabla \right) \nabla \phi \right] - \nabla \left(Ln + \frac{1}{B} \right) \cdot \widehat{\mathbf{b}} \times \nabla Ln$$
$$- \nabla \cdot \left(\widehat{\mathbf{b}} \times \nabla Ln \right) + O(\delta^3) = 0, \qquad (A.3)$$

or

$$\frac{\partial Ln}{\partial t} - \widehat{\mathbf{b}} \cdot \nabla \left(Ln + \frac{1}{B} \right) \times \nabla(\phi - Ln)$$
$$- \widehat{\mathbf{b}} \cdot \nabla \times \nabla(\phi - Ln) + O(\delta^3) = 0$$
$$\frac{\partial \nabla^2 \phi}{\partial t} + \nabla \cdot \left[\left(\widehat{\mathbf{b}} \cdot \nabla \phi \times \nabla \right) \nabla \phi \right] + \widehat{\mathbf{b}} \cdot \nabla \left(Ln + \frac{1}{B} \right)$$
$$\times \nabla Ln + \widehat{\mathbf{b}} \cdot \nabla \times \nabla Ln + O(\delta^3) = 0, \qquad (A.4)$$

or still

$$\frac{\partial Ln}{\partial t} - \left[Ln + \frac{1}{B}, \phi - Ln \right] + O(\delta^3) = 0$$
$$\frac{\partial \nabla^2 \phi}{\partial t} + \nabla \cdot [\phi, \nabla \phi] + \left[Ln + \frac{1}{B}, Ln \right] + O(\delta^3) = 0. \qquad (A.5)$$

Finally[5],

$$\frac{\partial Ln}{\partial t} - [Ln, \phi] - \left[\frac{1}{B}, \phi - Ln\right] + O(\delta^3) = 0$$

$$\frac{\partial \nabla^2 \phi}{\partial t} - \left[\nabla^2 \phi, \phi\right] + \left[\frac{1}{B}, Ln\right] + O(\delta^3) = 0, \quad \text{(A.6)}$$

which, given the form assumed for $1/B$, is equivalent to (2) if terms of order $O(\delta^3)$ and higher are neglected. The derivation given hereabove has the advantage of combining the fundamental physics contained in conservation equations with a formal, systematic expansion in a small parameter that enables strict control of the contribution of the different terms involved.

Appendix B. RK4 numerics

From a numerical point of view, (1) or (2) are discretised according to

$$\frac{dLn_{i,j}}{dt} = P\left[t, Ln_{i,j}(t), \nabla^2 \phi_{i,j}(t), \phi_{i,j}(t)\right]$$

$$\frac{d\nabla^2 \phi_{i,j}}{dt} = Q\left[t, Ln_{i,j}(t), \nabla^2 \phi_{i,j}(t), \phi_{i,j}(t)\right], \quad \text{(B.1)}$$

which are to be solved in the domain $[0,1] \times [0,1]$ and on an $N_1 \times N_2$ grid (of equally spaced points in $x_1 \times x_2$), with $u_{i,j}(t) = u_{\text{num}}(i/N_1, j/N_2, t)$ for some field $u(x_1, x_2, t)$ in the model, and given initial conditions $Ln_{i,j}(0)$ and $\phi_{i,j}(0)$. Equations (B.1) are advanced in time following the RK4 scheme [32]:

$$Ln_{i,j}(t + \Delta t) = Ln_{i,j}(t) + \frac{1}{6}\left(p_{1\,i,j} + 2p_{2\,i,j} + 2p_{3\,i,j} + p_{4\,i,j}\right)$$

$$\nabla^2 \phi_{i,j}(t + \Delta t) = \nabla^2 \phi_{i,j}(t) + \frac{1}{6}\left(q_{1\,i,j} + 2q_{2\,i,j} + 2q_{3\,i,j} + q_{4\,i,j}\right)$$

$$\phi_{i,j}(t + \Delta t) = \nabla^{-2}\left[\nabla^2 \phi_{i,j}(t + \Delta t)\right], \quad \text{(B.2)}$$

with ∇^{-2} the inverse Laplacian operator and

$$p_{1\,i,j} = P\left[t, Ln_{i,j}(t), \nabla^2 \phi_{i,j}(t), \phi_{i,j}(t)\right]\Delta t$$

$$q_{1\,i,j} = Q\left[t, Ln_{i,j}(t), \nabla^2 \phi_{i,j}(t), \phi_{i,j}(t)\right]\Delta t$$

$$\phi_{1\,i,j} = \nabla^{-2}\left[\nabla^2 \phi_{i,j}(t) + \frac{q_{1\,i,j}}{2}\right]$$

$$p_{2\,i,j} = P\left[t + \frac{\Delta t}{2}, Ln_{i,j}(t) + \frac{p_{1\,i,j}}{2}, \nabla^2 \phi_{i,j}(t) + \frac{q_{1\,i,j}}{2}, \phi_{1\,i,j}\right]\Delta t$$

$$q_{2\,i,j} = Q\left[t + \frac{\Delta t}{2}, Ln_{i,j}(t) + \frac{p_{1\,i,j}}{2}, \nabla^2 \phi_{i,j}(t) + \frac{q_{1\,i,j}}{2}, \phi_{1\,i,j}\right]\Delta t$$

$$\phi_{2\,i,j} = \nabla^{-2}\left[\nabla^2 \phi_{i,j}(t) + \frac{q_{2\,i,j}}{2}\right]$$

$$p_{3\,i,j} = P\left[t + \frac{\Delta t}{2}, Ln_{i,j}(t) + \frac{p_{2\,i,j}}{2}, \nabla^2 \phi_{i,j}(t) + \frac{q_{2\,i,j}}{2}, \phi_{2\,i,j}\right]\Delta t$$

$$q_{3\,i,j} = Q\left[t + \frac{\Delta t}{2}, Ln_{i,j}(t) + \frac{p_{2\,i,j}}{2}, \nabla^2 \phi_{i,j}(t) + \frac{q_{2\,i,j}}{2}, \phi_{2\,i,j}\right]\Delta t$$

$$\phi_{3\,i,j} = \nabla^{-2}\left[\nabla^2 \phi_{i,j}(t) + \frac{q_{3\,i,j}}{2}\right]$$

$$p_{4\,i,j} = P\left[t + \Delta t, Ln_{i,j}(t) + p_{3\,i,j}, \nabla^2 \phi_{i,j}(t) + q_{3\,i,j}, \phi_{3\,i,j}\right]\Delta t$$

$$q_{4\,i,j} = Q\left[t + \Delta t, Ln_{i,j}(t) + p_{3\,i,j}, \nabla^2 \phi_{i,j}(t) + q_{3\,i,j}, \phi_{3\,i,j}\right]\Delta t. \quad \text{(B.3)}$$

[5] Note that $\nabla \cdot [\phi, \nabla \phi] = \partial_1 [\phi, \partial_1 \phi] + \partial_2 [\phi, \partial_2 \phi] = [\partial_1 \phi, \partial_1 \phi] + [\partial_2 \phi, \partial_2 \phi] + [\phi, \partial_1^2 \phi] + [\phi, \partial_2^2 \phi] = [\phi, \nabla^2 \phi]$.

The derivative $\partial_1 u$ is numerically replaced by the fourth order central finite difference

$$\delta_1 u_{i,j}(t) = \frac{u_{i-2,j}(t) - 8u_{i-1,j}(t) + 8u_{i+1,j}(t) - u_{i+2,j}(t)}{12/(N_1 - 1)}, \quad \text{(B.4)}$$

with a similar expression, *mutatis mutandi*, for $\delta_2 u_{i,j}$ in substitution of $\partial_2 u$, and with this central finite difference algorithm implemented by simply shifting the $u_{i,j}(t)$ matrix and adding the resultant matrices multiplied by the respective coefficients, thus allowing simultaneous calculation of the field derivative in the entire domain, saving memory and computation time.

The third equation in (B.2) and three of the equations in (B.3) correspond to the inversion of Poisson's equation, which is carried out by discretising the Laplacian according to

$$\nabla^2 \phi_{i,j}(t) = \left(\delta_{11}^2 + \delta_{22}^2\right)\phi_{i,j}(t)$$

$$= -\frac{\phi_{i-2,j}(t) - 16\phi_{i-1,j}(t) + 30\phi_{i,j}(t) - 16\phi_{i+1,j}(t) + \phi_{i+2,j}(t)}{12/(N_1 - 1)^2}$$

$$- \frac{\phi_{i,j-2}(t) - 16\phi_{i,j-1}(t) + 30\phi_{i,j}(t) - 16\phi_{i,j+1}(t) + \phi_{i,j+2}(t)}{12/(N_2 - 1)^2} \quad \text{(B.5)}$$

and, using so-called natural ordering, writing the potential $\phi_{i,j}$ and the vorticity $\nabla^2 \phi_{i,j}$ in the form of vectors with $N_1 N_2$ entries each, respectively $\widetilde{\phi}_i$ and $\widetilde{\nabla^2 \phi}_i$, so the numerical Laplacian operator $\nabla^2_{i,j;i',j'}$ becomes an $N_1 N_2 \times N_1 N_2$ matrix $\widetilde{\nabla^2}_{i,j}$, yielding

$$\widetilde{\phi}_{i-1+j} = \phi_{i,j}$$

$$\widetilde{\nabla^2 \phi}_{i-1+j} = \nabla^2 \phi_{i,j}$$

$$\widetilde{\nabla^2}_{i-1+j,i'-1+j'} = \nabla^2_{i,j;i',j'}$$

$$= -\delta_{j,j'}\frac{\delta_{i-2,i'} - 16\delta_{i-1,i'} - 30\delta_{i,i'} - 16\delta_{i+1,i'} + \delta_{i+2,i'}(t)}{12/(N_1 - 1)^2}$$

$$- \delta_{i,i'}\frac{\delta_{j-2,j'} - 16\delta_{j-1,j'} + 30\delta_{j,j'} - 16\delta_{j+1,j'} + \delta_{j+2,j'}}{12/(N_2 - 1)^2}, \quad \text{(B.6)}$$

with $\delta_{i,j}$ the Kronecker delta. Equation (B.5) becomes

$$\widetilde{\nabla^2 \phi}_i = \widetilde{\nabla^2}_{i,j}\widetilde{\phi}_j, \quad \text{(B.7)}$$

where summation over repeated indices is assumed, (B.7) reading as a linear system of equations which, after adding appropriate boundary conditions (Dirichelet's or Neumann's) to its lhs, can be solved by standard methods.

With the use of fourth order central finite differences to emulate derivatives, one needs a frame around the integration domain of at least two 'ghost' grid points for the implementation of boundary conditions. The correct implementation of the latter is of particular importance when trying to numerically reproduce the analytical conservative solutions, which are time dependent and extend throughout the entire $x_1 \times x_2$ space, thus reaching beyond the $[0,1] \times [0,1]$ integration domain. Therefore, one has to deal with time evolving boundary conditions that must be sampled from the analytical solutions at the proper times. For instance, when computing

$p_{2\,0,j}$ and $q_{2\,0,j}$ in one of the intermediate steps in (B.3), a derivative one needs to estimate is $\partial_1 Ln$ at the boundary $x_1 = 0$ and

time $t + \Delta t/2$ which, according to (B.4), is replaced by

$$
\begin{aligned}
\delta_1 Ln_{0,j}\left(t + \Delta t/2\right) &= \frac{Ln_{-2,j}\left(t + \Delta t/2\right) - 8Ln_{-1,j}\left(t + \Delta t/2\right)}{12/\left(N_1 - 1\right)} + \frac{8Ln_{1,j}\left(t + \Delta t/2\right) - Ln_{2,j}\left(t + \Delta t/2\right)}{12/\left(N_1 - 1\right)} \\
&= \frac{Ln\left(-2/N_1, j/N_2, t + \Delta t/2\right) - 8Ln\left(-1/N_1, j/N_2, t + \Delta t/2\right)}{12/\left(N_1 - 1\right)} + \frac{8\left[Ln_{1,j}(t) + p_{1\,1,j}/2\right] - \left[Ln_{2,j}(t) + p_{1\,2,j}/2\right]}{12/\left(N_1 - 1\right)}.
\end{aligned}
$$

(B.8)

To provide a further example, the derivative $\partial_2 \nabla^2 \phi$ evaluated at $x_2 = N_2$ and $t + \Delta t$, as needed for $p_{4\,i,N_2}$ and $q_{4\,i,N_2}$, becomes

$$
\begin{aligned}
\delta_2 \nabla^2 \phi_{i,N_2}\left(t + \Delta t\right) &= \frac{\nabla^2 \phi_{i,N_2-2}\left(t + \Delta t\right) - 8\nabla^2 \phi_{i,N_2-1}\left(t + \Delta t\right)}{12/\left(N_2 - 1\right)} + \frac{8\nabla^2 \phi_{i,N_2+1}\left(t + \Delta t\right) - \nabla^2 \phi_{i,N_2+2}\left(t + \Delta t\right)}{12/\left(N_2 - 1\right)} \\
&= \frac{\left[\nabla^2 \phi_{i,N_2-2}(t) + q_{3\,i,N_2-2}\right] - 8\left[\nabla^2 \phi_{i,N_2-1}(t) + q_{3\,i,N_2-1}\right]}{12/\left(N_2 - 1\right)} + \frac{8\nabla^2 \phi\left(i/N_1, 1 + 1/N_2, t + \Delta t\right) - \nabla^2 \phi\left(i/N_1, 1 + 2/N_2, t + \Delta t\right)}{12/\left(N_2 - 1\right)}.
\end{aligned}
$$

(B.9)

The same care with boundary conditions sampled from analytical solutions applies to the computation of the Laplacian in (B.5) as, for instance, when calculating $\nabla^2 \phi$ for $x_1 = 1$ and $x_2 = 0$ at time $t + \Delta t/2$ to retrieve $\phi_{1\,i,j}$ appearing in (B.3):

$$
\begin{aligned}
\nabla^2 \phi_{N_1,0}(t) + \frac{q_{1\,N_1,0}}{2} &= -\frac{\phi_{N_1-2,0}\left(t + \Delta t/2\right) - 16\phi_{N_1-1,0}\left(t + \Delta t/2\right) + 30\phi_{N_1,0}\left(t + \Delta t/2\right)}{12/\left(N_1 - 1\right)^2} \\
&\quad + \frac{16\phi_{N_1+1,0}\left(t + \Delta t/2\right) - \phi_{N_1+2,0}\left(t + \Delta t/2\right)}{12/\left(N_1 - 1\right)^2} - \frac{\phi_{N_1,-2}\left(t + \Delta t/2\right) - 16\phi_{N_1,-1}\left(t + \Delta t/2\right)}{12/\left(N_2 - 1\right)^2} \\
&\quad - \frac{30\phi_{N_1,0}\left(t + \Delta t/2\right) - 16\phi_{N_1,1}\left(t + \Delta t/2\right) + \phi_{N_1,2}\left(t + \Delta t/2\right)}{12/\left(N_2 - 1\right)^2} \\
&= -\frac{\phi_{1\,N_1-2,0} - 16\phi_{1\,N_1-1,0} + 30\phi_{1\,N_1,0}}{12/\left(N_1 - 1\right)^2} + \frac{16\phi\left(1 + 1/N_1, 0, t + \Delta t/2\right) - \phi\left(1 + 2/N_1, 0, t + \Delta t/2\right)}{12/\left(N_1 - 1\right)^2} \\
&\quad - \frac{\phi\left(1, -2/N_2, t + \Delta t/2\right) - 16\phi\left(1, -1/N_2, t + \Delta t/2\right)}{12/\left(N_2 - 1\right)^2} - \frac{30\phi_{1\,N_1,0} - 16\phi_{1\,N_1,1} + \phi_{1\,N_1,2}}{12/\left(N_2 - 1\right)^2}.
\end{aligned}
$$

(B.10)

Moving the analytically retrieved boundary conditions to the lhs of (B.10), the latter can be rewritten in a form more appropriate for inverting Poisson's equation as

$$
\begin{aligned}
\nabla^2 \phi_{N_1,0}(t) + \frac{q_{1\,N_1,0}}{2} &- \frac{16\phi\left(1 + 1/N_1, 0, t + \Delta t/2\right) - \phi\left(1 + 2/N_1, 0, t + \Delta t/2\right)}{12/\left(N_1 - 1\right)^2} \\
&+ \frac{\phi\left(1, -2/N_2, t + \Delta t/2\right) - 16\phi\left(1, -1/N_2, t + \Delta t/2\right)}{12/\left(N_2 - 1\right)^2} \\
&= -\frac{\phi_{1\,N_1-2,0} - 16\phi_{1\,N_1-1,0} + 30\phi_{1\,N_1,0}}{12/\left(N_1 - 1\right)^2} - \frac{30\phi_{1\,N_1,0} - 16\phi_{1\,N_1,1} + \phi_{1\,N_1,2}}{12/\left(N_2 - 1\right)^2}.
\end{aligned}
$$

(B.11)

Appendix C. Order of accuracy check

A further trial on the proper implementation of the numerical algorithm can be conducted, specifically addressed at testing the order of convergence p of the truncation error resulting from the discretisation scheme applied to the model equations. In the present case, using an RK4 scheme for advancing equations in time together with fourth order central finite differences in space, one expects the truncation error in some numerical field estimate $u_{\text{num}}(x_1, x_2, t)$ to obey [31, 35]

$$
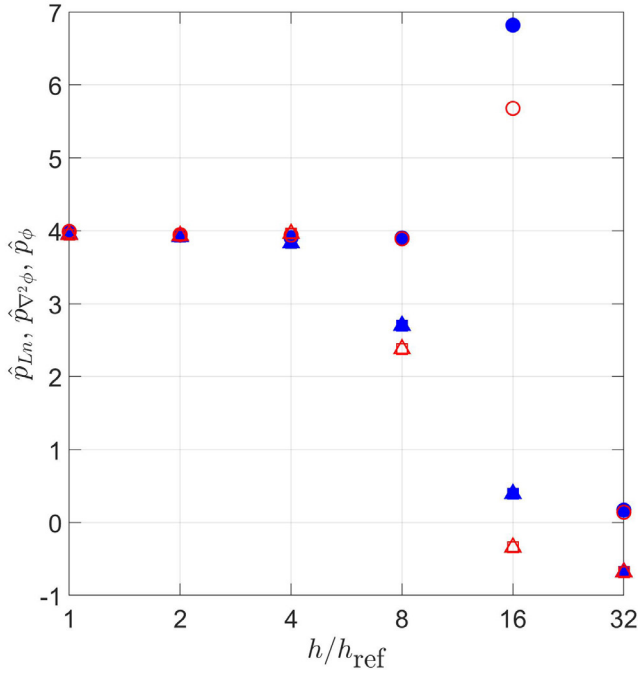\varepsilon_u^{(h)} \approx Eh^4,
$$

(C.1)

Figure C1. Observed orders of accuracy $\hat{p}_{Ln}(h)$ (triangles), $\hat{p}_{\nabla^2\phi}(h)$ (squares) and $\hat{p}_\phi(h)$ (circles), using norms (C.3) (blue, full symbols) and (C.4) (red, open symbols), for the numerical logarithmic density, vorticity and electrostatic potential plotted in figure 9.
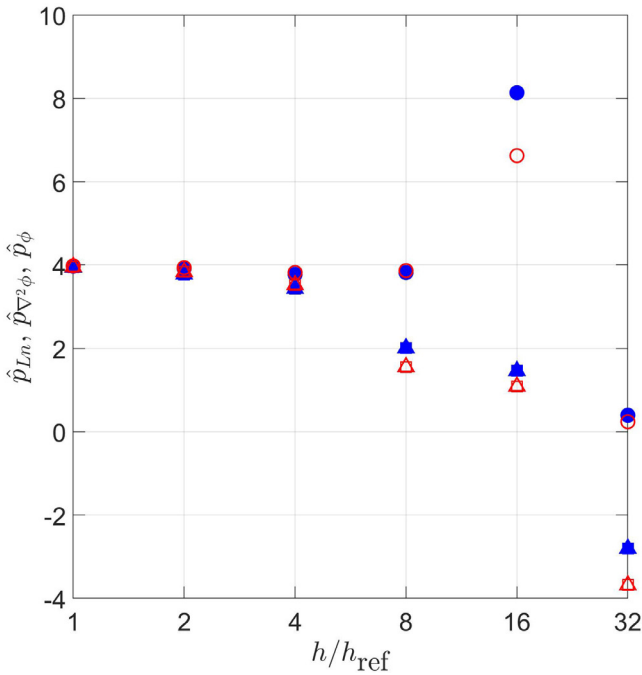

Figure C2. Observed orders of accuracy $\hat{p}_{Ln}(h)$ (triangles), $\hat{p}_{\nabla^2\phi}(h)$ (squares) and $\hat{p}_\phi(h)$ (circles), using norms (C.3) (blue, full symbols) and (C.4) (red, open symbols), for the numerical logarithmic density, vorticity and electrostatic potential plotted in figure 10.

where E is some coefficient independent of the generalised mesh size $h = \Delta x_1 = \Delta x_2 = \Delta t$, with $\Delta x_1 = 1/(N_1 - 1)$, $\Delta x_2 = 1/(N_2 - 1)$ and $\Delta t = t_{sim}/N_t$ varying with the number N_t of time steps for a fixed simulation running time t_{sim} (excluding the initial $t = 0$ step, whose contribution to the
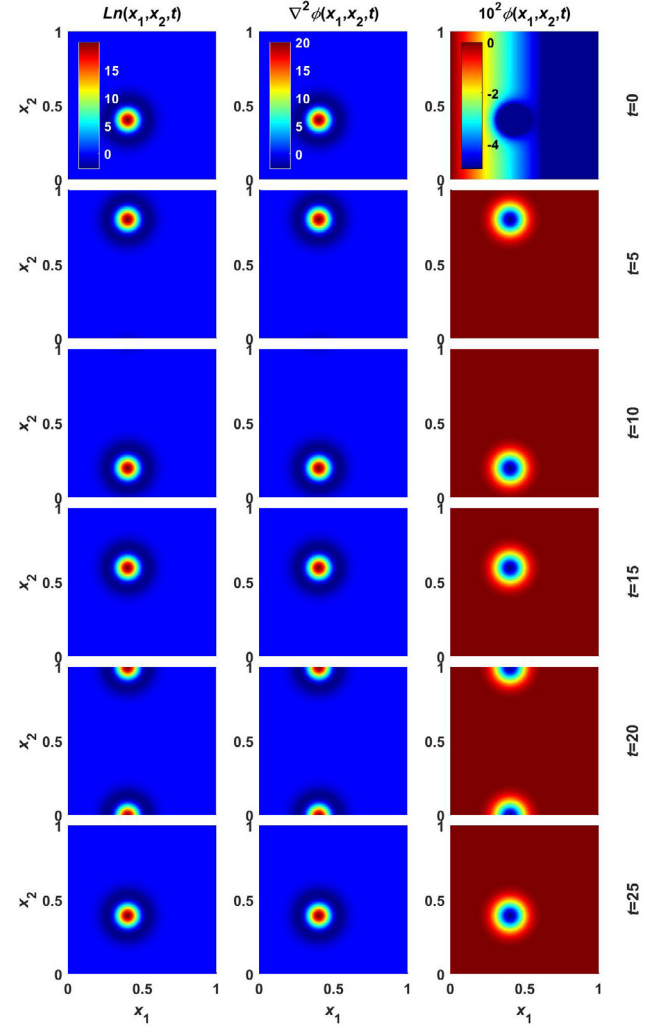

Figure D1. Snapshots with contour plots of the numerical logarithmic density $Ln(x_1, x_2, t)$, vorticity $\nabla^2\phi(x_1, x_2, t)$ and electrostatic potential $\phi(x_1, x_2, t)$, for the same conditions and parameters as in figure 12, but for zero boundary conditions in x_1 and periodic boundary conditions in x_2.

error obviously vanishes). Suppose, now, one coarsens the mesh by some factor r, meaning h is replaced by rh, and subsequently computes the quantity

$$\hat{p}_u = \frac{\ln\left(\varepsilon_u^{(rh)}/\varepsilon_u^{(h)}\right)}{\ln r};$$
(C.2)

then, according to (C.1), one presumes $\hat{p}$ to converge to 4 when h is made smaller and smaller. If such is the case, one can safely say that model equations are correctly solved within the order of accuracy expected for the numerical scheme. To perform this order of accuracy test, the errors $\varepsilon_u^{(h)}$ in the different fields have been estimated using the following two norms:

$$\varepsilon_u^{(h)} = L_{1u}^{(h)} = \frac{1}{N_1 N_2 N_t} \sum_{i=0}^{N_1} \sum_{j=0}^{N_2} \sum_{l=1}^{N_t} \epsilon_u\left(i/N_1, j/N_2, lt_{sim}/N_t\right)$$
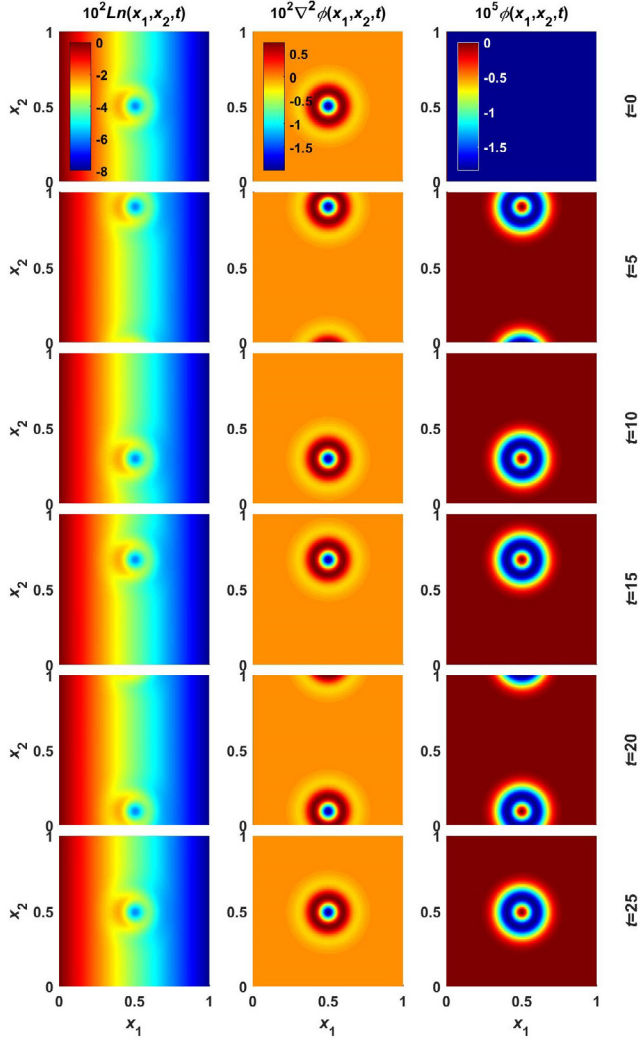(C.3)

and

Figure D2. Snapshots with contour plots of the numerical logarithmic density $Ln(x_1, x_2, t)$, vorticity $\nabla^2 \phi(x_1, x_2, t)$ and electrostatic potential $\phi(x_1, x_2, t)$, for the same conditions and parameters as in figure 13, but for zero boundary conditions in x_1 and periodic boundary conditions in x_2.

$$\varepsilon_u^{(h)} = L_{2u}^{(h)} = \sqrt{\frac{1}{N_1 N_2 N_t} \sum_{i=0}^{N_1} \sum_{j=0}^{N_2} \sum_{l=1}^{N_t} \epsilon_u^2 (i/N_1, j/N_2, lt_{sim}/N_t)},$$

(C.4)

which correspond, respectively, to the simple and the root square means of the local error defined in (18).

So, taking as reference $h_{ref} = 0.005$ for the finest mesh tested, coarsening has been implemented according to $h = r^p h_{ref}$, with $r = 2$ and $p = 0, 1, 2, 3, 4, 5$, making $t_{sim} = 10$, and simulations have been run for the two localised solutions shown in figures 9 and 10. The outcome for the different $\hat{p}_u$ is plotted in figures C1 and C2, and convergence to the theoretically expected order of accuracy $\hat{p}_u = 4$ is clearly observed for all fields pertaining to the two solutions and for
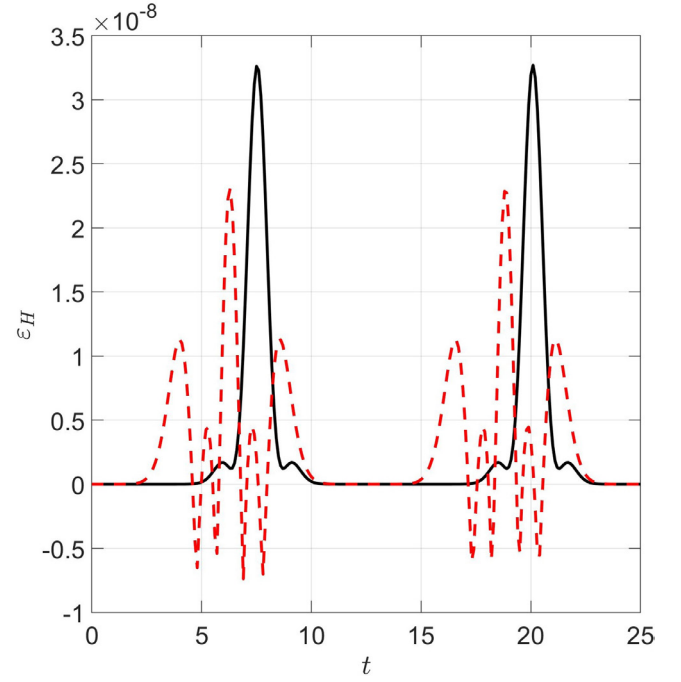

Figure D3. Relative error $\varepsilon_H(t)$ in the conservation of H for the same conditions and parameters as in figures D1 (black, solid line) and D2 (red, dashed line).

both norms (C.3) and (C.4), reinforcing one's confidence in the numerical implementation of SOL models (1) and (2).

Appendix D. Numerical dissipation test

It is possible to show that, for the conservative model (2), provided the boundary terms vanish,

$$H = \frac{1}{2} \int \int dx_1 dx_2 \left(Ln^2 + |\nabla \phi|^2 \right)$$

(D.1)

is a conserved quantity; actually the Hamiltonian which, together with an appropriate Poisson bracket, defines a Hamiltonian structure of the Lie–Poisson type [29], and the same quantity H that also obeys an energy-like theorem in the Hasegawa–Wakatani model [8]. Indeed, combining (2) and (D.1), and dropping all boundary terms arising when integrating, follows [24]

$$\frac{d}{dt} \frac{1}{2} \int \int dx_1 dx_2 Ln^2 + \int \int dx_1 dx_2 g \phi \partial_2 Ln$$
$$= \int \int dx_1 dx_2 Ln \frac{\partial Ln}{\partial t} + \int \int dx_1 dx_2 g \phi \partial_2 Ln$$
$$= -\widehat{\mathbf{b}} \cdot \int \int dx_1 dx_2 \nabla \phi \times \nabla Ln$$
$$= \widehat{\mathbf{b}} \cdot \int \int dx_1 dx_2 \phi \nabla \times \nabla Ln = 0$$

(D.2)

and

$$\frac{\mathrm{d}}{\mathrm{d}t}\frac{1}{2}\int\int \mathrm{d}x_1\mathrm{d}x_2 \left|\nabla\phi\right|^2 - \int\int \mathrm{d}x_1\mathrm{d}x_2 g\phi\partial_2 Ln$$

$$= -\int\int \mathrm{d}x_1\mathrm{d}x_2\phi\frac{\partial\nabla^2\phi}{\partial t} - \int\int \mathrm{d}x_1\mathrm{d}x_2 g\phi\partial_2 Ln$$

$$= \widehat{\mathbf{b}}\cdot\int\int \mathrm{d}x_1\mathrm{d}x_2\phi\nabla\phi\times\nabla\nabla^2\phi$$

$$= \widehat{\mathbf{b}}\cdot\int\int \mathrm{d}x_1\mathrm{d}x_2\nabla^2\phi\nabla\times(\phi\nabla\phi) = 0, \qquad (D.3)$$

hence

$$\frac{\mathrm{d}H}{\mathrm{d}t} = 0. \qquad (D.4)$$

Boundary terms in the integrations above vanish either because they do become zero, or because they cancel each other, which corresponds to imposing vanishing or periodic boundary conditions, respectively. Therefore, the same initial conditions used to numerically run (2) and obtain figures 12 and 13 have been used to test (D.4) with vanishing boundary conditions in x_1 and periodic in x_2, applied to all three functions Ln, $\nabla^2\phi$ and ϕ, the results of this exercise being shown in figures D1 and D2, with the corresponding error in numerical dissipation, defined as

$$\varepsilon_H = \frac{H\left(t\right) - H\left(0\right)}{H\left(0\right)}, \qquad (D.5)$$

being plotted in figure D3. One sees that numerical dissipation, as measured by ε_H, is indeed kept under tight control, remaining perfectly negligible at all times, always below 3.5×10^{-8}, the periodic peaks being correlated with the crossing of the periodic boundary in x_2 by the blob- and hole-like structures (and its reappearance at $x_2 = 0$), as can be verified by checking the times in figures D1–D3[6].

---

[6] Note that the peaks in figure D3 do not come from the numerical solution of model (2), but arise from the calculation of the quantity H defined in (D.1), being probably due to the computation of $\nabla\phi$ at boundary points.

ORCID iDs

João P.S. Bizarro ⬤ https://orcid.org/0000-0002-0698-6259

References

[1] Sarazin Y. and Ghendrih Ph. 1998 *Phys. Plasmas* **5** 4214
[2] Ghendrih Ph. *et al* 2003 *Nucl. Fusion* **43** 1013
[3] Garcia O.E. *et al* 2004 *Phys. Rev. Lett.* **92** 165003
[4] Bisai N. *et al* 2004 *Phys. Plasmas* **11** 4018
[5] Bisai N. *et al* 2005 *Phys. Plasmas* **12** 102515
[6] Garcia O.E. *et al* 2006 *Phys. Plasmas* **13** 082309
[7] Zweben S.J. *et al* 2007 *Plasma Phys. Control. Fusion* **49** S1
[8] Naulin V. 2007 *J. Nucl. Mater.* **363–5** 24
[9] Krasheninnikov S.I. *et al* 2008 *J. Plasma Phys.* **74** 679
[10] Furno I. *et al* 2008 *Phys. Rev. Lett.* **100** 055004
[11] Boedo J.A. 2009 *J. Nucl. Mater.* **390–1** 29
[12] Theiler C. *et al* 2009 *Phys. Rev. Lett.* **103** 065001
[13] D'Ippolito D.A. *et al* 2011 *Phys. Plasmas* **18** 060501
[14] Angus J.R. *et al* 2012 *Phys. Plasmas* **19** 082312
[15] Myra J.R. *et al* 2013 *Nucl. Fusion* **53** 073013
[16] Kendl A. 2015 *Plasma Phys. Control. Fusion* **57** 045012
[17] Riva F. *et al* 2016 *Plasma Phys. Control. Fusion* **58** 044005
[18] Olsen J. *et al* 2016 *Plasma Phys. Control. Fusion* **58** 044011
[19] Halpern F.D. *et al* 2016 *J. Comput. Phys.* **315** 388
[20] Krasheninnikov S.I. 2001 *Phys. Lett.* A **283** 368
[21] Pécseli H.L. *et al* 2016 *Plasma Phys. Control. Fusion* **58** 104002
[22] Bodi K. *et al* 2014 *Contrib. Plasma Phys.* **48** 63
[23] Krasheninnikov S.I. 2016 *Phys. Lett.* A **380** 3905
[24] Vilela Mendes R. and Bizarro J.P.S. 2017 *Phys. Plasmas* **24** 012303
[25] Vilela Mendes R. and Duarte J.T. 1981 *J. Math. Phys.* **22** 1420
[26] Duarte J.T. and Vilela Mendes R. 1983 *J. Math. Phys.* **24** 1772
[27] Figarella C.F. *et al* 2005 *J. Nucl. Mater.* **337–9** 342
[28] Colin C. *et al* 2014 *Contrib. Plasma Phys.* **54** 543
[29] Izacard O. *et al* 2011 *Phys. Plasmas* **18** 062105
[30] Riva F. *et al* 2017 *Plasma Phys. Control. Fusion* **59** 035001
[31] Riva F. *et al* 2014 *Phys. Plasmas* **21** 062301
[32] Press W. *et al* 2007 *Numerical Recipes* 3rd edn (Cambridge: Cambridge University Press)
[33] Bizarro J.P. and Moreau D. 1993 *Phys. Fluids* B **5** 1227
[34] Bizarro J.P.S. *et al* 2016 *Plasma Phys. Control. Fusion* **58** 105010
[35] Oberkampf W. and Roy C. 2010 *Verification and Validation in Scientific Computing* (Cambridge: Cambridge University Press)